

# Spatiotemporal distribution and influencing factors of impervious surface evaporation in the Baiyangdian catchment from 1980 to 2020

Xiaoyu Liu<sup>1,2</sup>  | Xingguo Mo<sup>1,2,3</sup> | Suxia Liu<sup>1,2,3</sup> | Shi Hu<sup>1</sup>

<sup>1</sup>Key Laboratory of Water Cycle and Related Land Surface Processes, Institute of Geographic Sciences and Natural Resources Research, Chinese Academy of Sciences, Beijing, China

<sup>2</sup>College of Resources and Environment, University of Chinese Academy of Sciences, Beijing, China

<sup>3</sup>Sino-Danish Center, University of Chinese Academy of Sciences, Beijing, China

## Correspondence

Xingguo Mo, Key Laboratory of Water Cycle and Related Land Surface Processes, Institute of Geographic Sciences and Natural Resources Research, Chinese Academy of Sciences, 11A, Datun Road, Chaoyang, Beijing 100101, China.  
 Email: [moxg@igsnrr.ac.cn](mailto:moxg@igsnrr.ac.cn)

## Funding information

National Key Research and Development Program of China, Grant/Award Numbers: 2022YFF0801804, 2018YFE0106500

## Abstract

Evaporation from impervious surfaces plays a vital role in the catchment water cycle. Exploring the spatiotemporal variation patterns and influencing mechanisms of impervious surface evaporation at the catchment scale can improve the understanding and evaluation of the evaporation process. This study downloaded 0.5 m resolution images of the Baiyangdian catchment (BYD) from Google Earth and used deep learning to identify impervious surfaces. This was used to revise impervious surfaces of the China land cover dataset in 1985 and 1990–2020. Potential evaporation (PET) from three types of impervious surfaces (roofs, ground affected or not affected by the building height) was calculated by modifying the parameters of the Penman–Monteith equation, and daily precipitation and water-storage capacity of impervious surfaces were taken into account to estimate impervious surface evaporation ( $E$ ). The results showed that  $E$  values of the three types of impervious surfaces were between 72.1 and 178.2 mm/year and all exhibited the spatial distribution of high in the northwest and low in the southeast of the BYD in 1980–2020. Compared with that in 1980, in 2020, the cumulative evaporation (EAP) increased by 134.4%. The ratio of EAP to cumulative precipitation ranged from 3.0% to 6.9%, increasing significantly in a fluctuating manner. The increments in precipitation days and impervious surface area played a major role in the increase of EAP, and the decrease in precipitation was the fundamental reason for the increase in the proportion of impervious surface evaporation and water resource pressure in the BYD. Excluding the continuous evaporation from the remaining water can likely lead to underestimating the impervious surface evaporation. This study provides an efficient and reasonable novel approach for calculating impervious surface evaporation in long series and large-scale catchments.

## KEY WORDS

Baiyangdian catchment, impervious surface, impervious surface evaporation, potential evaporation, precipitation

## 1 | INTRODUCTION

Changes in land cover and the rapid expansion of impervious surfaces directly or indirectly affect water cycle processes, such as

evaporation, runoff and infiltration in the catchment, and have a substantial impact on the catchment water balance (Strohbach et al., 2019; Wang, Onodera, et al., 2021). Impervious surfaces are hardened artificial surfaces paved with concrete, asphalt and other

materials. This artificial material cuts off the hydrological connection between surface water and groundwater and prevents the infiltration process, leading to increased runoff (Dams et al., 2013; Zhang et al., 2018) and a substantial increase in water production during the monsoon (Wagner et al., 2016). Meanwhile, the conversion of the natural landscape to impervious surfaces can result in a decrease in evaporation and an increase in groundwater recharge rates (Minnig et al., 2018; Wagner et al., 2016). Impervious surfaces connect the natural landscape and water bodies and have a certain water-storage capacity (Boyd et al., 1993; Omidvar et al., 2018; Willuweit & O'Sullivan, 2013) and evaporation processes. The evaporation rate of impervious surfaces in the wet state is higher than that of the vegetation-covered surface. Although evaporation of impervious surfaces is intermittent, it accounts for nearly 18% of the total latent heat flux (LE) after 10 days of relatively wet conditions (Ramamurthy & Bou-Zeid, 2014), and 16%–29% of the total amount of evaporation from impervious surfaces in urban built-up areas (Zhou et al., 2021). In Helsinki, Finland, the evaporation of impervious areas was as high as 835 m<sup>3</sup>/ha/a, which significantly affected the urban water balance and ecosystem service value of urban green spaces (Silvennoinen et al., 2017).

However, to date, compared with the natural environment, the evaporation of impervious surfaces has rarely been observed and can be difficult to monitor (Ramamurthy & Bou-Zeid, 2014). Therefore, the evaporation of impervious surfaces is often underestimated or excluded from researches. Methods of impervious surface evaporation can be divided into three types. The first method involves field measurements. Eddy covariance (EC) technology is widely used to monitor evapotranspiration (ET) in natural and urban areas. However, owing to the highly heterogeneous urban surface, removing the influence of urban vegetation and soil ET and accurately extracting impervious surface evaporation is a technical challenge. EC technology also has spatiotemporal limitations; it lacks data collected during historical periods and cannot be used for large-scale data analyses (Chen et al., 2023). The second method uses an empirical model. Based on experiments and urban design regulations (Zhou et al., 2021), the empirical model only considers the relationship between the water storage capacity of impervious surfaces (Moravej et al., 2020) and daily precipitation. It uses a simple mathematical formula to estimate the evaporation of impervious surfaces (Zhou et al., 2019). This requires less hydrological data, and focuses more on the overall condition of a catchment. Therefore, the empirical model is suitable for larger temporal and spatial scales, but the model does not consider the energy-driven evaporation process. Thus, if radiation and aerodynamic factors are not considered, the calculated impervious surface evaporation may be overestimated. Willuweit and O'Sullivan (2013) identified this problem, and compared the potential ET of the day and the water storage depth of impervious surfaces to estimate impervious surface evaporation. However, the roughness, albedo and other parameters of impervious surfaces are different from those of natural surfaces. Selecting accurate parameters improves the estimation accuracy of evaporation of impervious surfaces. The third method is an urban evaporation model with a physical mechanism, typically the

urban canopy model (Liu et al., 2017; Ramamurthy & Bou-Zeid, 2014; Wang et al., 2011) and the urban evaporation interception model (Grimmond & Oke, 1991). The Surface Urban Energy and Water Balance Scheme (SUEWS) model was developed on the urban evaporation interception model (Cleugh et al., 2005; Järvi et al., 2011; Wiegels et al., 2021). These models consider that the complex geometry of buildings allows for more complex turbulent movements within the urban canopy (Oke, 1976). Changes in the urban underlying surface roughness and wind field because of building height are important factors affecting evaporation from impervious surfaces (Mahat et al., 2013; Masson, 2000; Meili et al., 2020). However, excessive input parameters limit the use of such models in medium and large catchments. Therefore, when the regional scale of the research object is relatively large and the time series is relatively long, it is necessary to fully consider the effect of urban form on the physical mechanism of evaporation from impervious surfaces and the water storage capacity of impervious surfaces, ensuring the simplicity and efficiency of the calculation process.

The Baiyangdian catchment (BYD) is located in the middle of the North China Plain and is part of the Haihe River catchment. With increasing urbanization in the catchment, there has been considerable impact from human activities, and the catchment currently has extensive human-water conflict (Wang, Lv, & Zhang, 2021). Appropriate management and allocation of scarce water resources in the catchment has become an important issue (Yang & Yang, 2014). In recent decades, the temperature in the catchment has shown an upward trend. However, the change in precipitation has not been significant. Potential ET in most areas of the catchment have increased significantly, whereas ET around built-up areas has shown a weakening trend (Chen et al., 2022). Urban areas have high sensible heat flux due to factors such as low vegetation cover and high impermeability, and the actual evaporation of impervious surfaces is less than 200 mm (Guo & Shen, 2015). Although the expansion of impervious surfaces has exacerbated the vulnerability of the BYD ecosystem (Kuang et al., 2013), and changes in hydrological cycle processes have brought about uncertainty in water allocation, impervious surface evaporation has attracted insufficient attention. Given that impervious surface evaporation is a critical link in the catchment hydrological cycle, its calculation method requires further improvement, and the influencing factors need to be determined. The temporal and spatial variation patterns of impervious surface evaporation in catchments need to be examined. Meanwhile, there are significant differences in information interpretation and spatial resolution of diverse types of land use data. Geometric registration and classification errors of land-use pixels (Ackerman & Stein, 2008) have rendered some land-use data unable to parameterize urban areas correctly (Dams et al., 2013) and meet the needs of mesoscale hydrological models (Montzka et al., 2008). Different area ratios are assigned to the main land cover types, including forests, grasslands, water bodies and impervious surfaces (Wegehenkel et al., 2006), and significantly affect the results of urban hydrological modelling (Chen et al., 2023; Wegehenkel et al., 2006; Zipper et al., 2017). This has further emphasized that accurate land use information is critical for accurate urban

evaporation model results (Cheng & Byun, 2008). Therefore, in this study, the relevant parameters in the Penman–Monteith equation were modified based on the building height to calculate the daily potential evaporation (PET) from impervious surfaces. Considering daily precipitation, daily PET, the water storage capacity of impervious surfaces, and revised land use data, impervious surface evaporation was estimated for the BYD. This study analysed the spatiotemporal distribution and influencing factors of impervious surface evaporation by using long-term sequencing to provide a scientific basis for the management and allocation of water resources in the BYD.

## 2 | MATERIALS AND METHODS

### 2.1 | Study area

The BYD is located in North China ( $113.65^{\circ}$ – $116.50^{\circ}$  E,  $38.02^{\circ}$ – $40.06^{\circ}$  N), with a total area of  $3.56 \times 10^4$  km $^2$  (Figure 1). The BYD forms a part of the temperate and East Asian monsoon climate zones with four distinct seasons, including cold winters and high-temperature and rainy summers. The average precipitation from 1980 to 2020 was 366–775 mm/year.

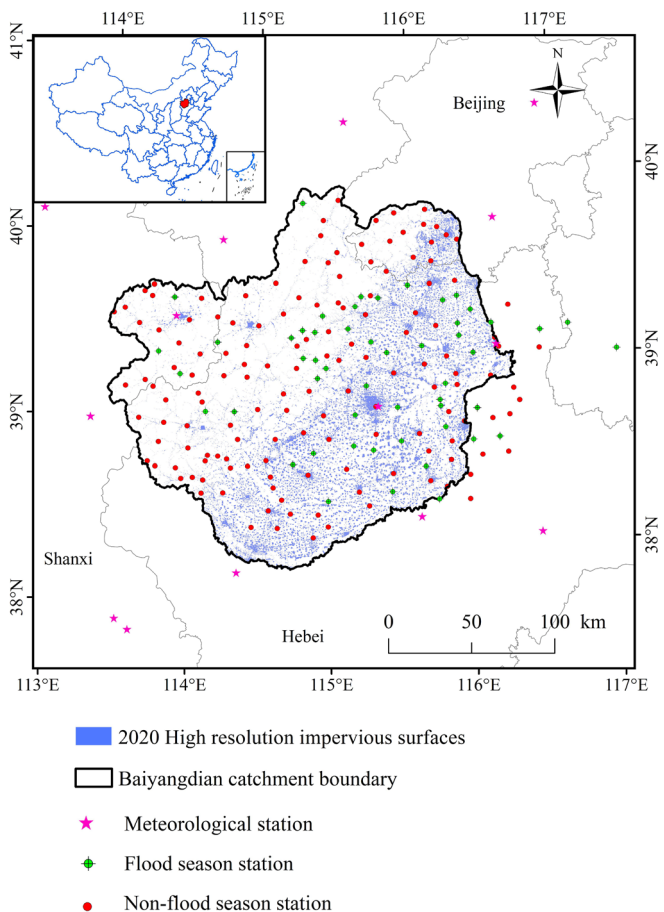


**FIGURE 1** Geographical location, boundary and station distribution of the Baiyangdian catchment (BYD).

### 2.2 | Datasets

#### 2.2.1 | High-resolution impervious data from remote sensing images

High-resolution remote sensing images from 2020 were obtained using Google Earth. Remote sensing images with 0.5 m resolution were downloaded and interpreted visually and manually. Building roofs, roads and construction land were extracted using deep learning semantic segmentation. The evaluation indicator for data accuracy was the Intersection over Union (IoU). This represents the ratio of the IoU between the region obtained using the semantic segmentation method and the actual region. The mean IoU in the semantic segmentation task is the mean Intersection over Union (mIoU). In this study, the identification accuracies—of the building roof mIoU = 0.8550, construction land mIoU = 0.8475 and roads mIoU = 0.8462—were relatively high. These three categories were combined into high-resolution impervious data (HR).

#### 2.2.2 | Meteorological data and DEM

Meteorological station data from 1980 to 2020 were obtained from the China Meteorological Administration (<http://data.cma.cn/>). This included daily precipitation, average temperature, wind speed, relative humidity, sunshine duration and atmospheric pressure data. The study supplemented rainfall station data, making the distribution of precipitation stations more uniform. Daily precipitation data from 2006 to 2020 were obtained from the Haihe River Catchment Hydrological Yearbook. The 30 m resolution Digital Elevation Model (DEM) data was sourced from the Shuttle Radar Topography Mission (SRTM), and resampled to 250 m. Anusplin software was used to perform cubic spline interpolation of meteorological data—based on DEM data—to obtain raster data with a resolution of 250 m.

#### 2.2.3 | Land use data

Compared with other land use data, the China land cover dataset has the advantage of data coherence, long time series with a high resolution of 30 m. The China land cover dataset was selected from 1985 and 1990 to 2020 (Yang & Huang, 2022). The land use type ‘impervious’ was extracted and expressed as CLCD.

Given the lack of CLCD data from 1980 to 1984 and 1986 to 1989, the CLCD data from 1985 were used to assign CLCD data from 1980 to 1984. The CLCD data from 1990 were used to assign CLCD data from 1986 to 1989.

#### 2.2.4 | Building height

The 2020 China building height data were downloaded at 10 m resolution (Wu, 2023; Wu et al., 2023a,b) and converted to the average

building height at 250 m resolution. However, there was a lack of historical building height data. To obtain the average building height data from the same time series as the CLCD data, reference was made to the residential building design regulations implemented in 1987. These regulations stated that residential floor height should not be higher than 2.8 m. Historical urban photos in the BYD showed that 1–3 floors are common. Meanwhile, the 1 km data from 2015 (Li et al., 2020) and the 30 m data from 2010 (Huang et al., 2022) are different from the 10 m data (Wu, 2023; Wu et al., 2023a,b). To avoid the influence of different data sources and resolutions, it was assumed that the average building height with a resolution of 250 m in the BYD in 1985 was 5 m. The 32 years (1985, 1990–2020) were considered as independent variables. Building height was the dependent variable. A regression equation was established, and building height data at 250 m resolution for the 32 years were obtained. The building height data in 1985 were used to assign the data from 1980 to 1984, and the building height data from 1990 were used to assign the data from 1986 to 1989.

## 2.3 | Methods

### 2.3.1 | Wind speed and aerodynamic resistance

Referring to the research by Wouters et al. (2015) and Sarkar and De Ridder (2011):

$$z_{om,urban} = 0.075H, \quad (1)$$

$$d_{urban} \cong 10z_{om,urban}, \quad (2)$$

where  $d_{urban}$  is the urban canopy displacement height (m),  $z_{om,urban}$  is the urban canopy roughness length (m),  $H$  is the average building height (m).

The roughness length governing the transfer of heat and vapour  $z_{oh,urban}$  (m) can be approximated as (Allen et al., 1998):

$$z_{oh,urban} = 0.1z_{om,urban}. \quad (3)$$

In areas where the building height is greater than 0, the impact of buildings on wind speed needs to be considered. Therefore, it is assumed that the wind speed profile is logarithmic above the average height of urban buildings  $H$  and exponential from height  $H$  to the ground (Mahat et al., 2013; Masson, 2000; Meili et al., 2020).

$$u(z) = \frac{1}{k} u_{atm}^* \ln\left(\frac{z - d_{urban}}{z_{om,urban}}\right) \text{ for } Z_{atm} \geq z \geq H, \quad (4)$$

$$u(z) = u_H \exp\left(-\hat{\beta}\left(1 - \frac{z}{H}\right)\right) \text{ for } H > z, \quad (5)$$

$$u_H = \frac{1}{k} u_{atm}^* \ln\left(\frac{H - d_{urban}}{z_{om,urban}}\right), \quad (6)$$

where  $k$  is the von Karman constant, 0.4 (–),  $z$  is the calculated height (m) and  $Z_{atm}$  is the atmospheric reference height (m), which is the average height of the building plus wind speed measurement (10 m).  $\hat{\beta}$  is the attenuation coefficient (–),  $Z_{ground,ref}$  is the reference height near the ground (ground affected by the building height, abbreviated as GH) and equals 2 m.  $Z_{roof,ref}$  is the roof reference height (m). The roof height is equal to the average height of the buildings.  $u_H$  is the wind speed at the average height of the urban buildings ( $m s^{-1}$ ) and  $u_{atm}^*$  is the friction speed ( $m s^{-1}$ ), which is calculated as follows:

$$Z_{roof,ref} = H + 2, \quad (7)$$

$$u_{atm}^* = \frac{k u_{atm}}{\ln(Z_{atm} - d_{urban}) / (z_{om,urban})}, \quad (8)$$

where  $u_{atm}$  is the wind speed at the atmospheric reference height ( $m s^{-1}$ ). The attenuation coefficient  $\hat{\beta}$  is calculated as follows (Meili et al., 2020):

$$\hat{\beta} = \frac{\ln[u_{atm}/u_H]}{Z_{atm}/H - 1}. \quad (9)$$

The wind speed in the area where the building height is 0 is not affected by the building, and  $U_2$  in FAO56 is used as the wind speed in these areas. Ground not affected by the building height is abbreviated as G0.

$$U_2 = U_{10} \frac{4.87}{\ln(67.8 \times 10 - 5.42)}. \quad (10)$$

### 2.3.2 | Impervious surface evaporation

$$PET = \frac{\Delta(R_n - G)}{\lambda(\Delta + \gamma)} + \frac{r_a}{\lambda(\Delta + \gamma)}, \quad (11)$$

where PET is the potential evaporation ( $mm day^{-1}$ ),  $R_n$  is the net radiation ( $MJ m^{-2} day^{-1}$ ),  $G$  is the heat stored in the water ( $MJ m^{-2} day^{-1}$ ) and equals  $0.1R_n$ ,  $(e_s - e_a)$  is the saturation vapour pressure deficit (kPa).  $\rho_a$  is the mean air density at constant pressure ( $kg m^{-3}$ ).  $C_p$  is the specific heat of air ( $MJ kg^{-1} ^\circ C^{-1}$ ).  $\lambda$  is the latent heat of vaporization ( $MJ kg^{-1}$ ),  $\Delta$  is the slope of the relationship between the saturated vapour pressure and temperature ( $kPa ^\circ C^{-1}$ ),  $\gamma$  is the psychrometric constant ( $kPa ^\circ C^{-1}$ ) and  $r_a$  is the aerodynamic resistance ( $s m^{-1}$ ).

$$r_a = \frac{\ln\left[\frac{Z_m - d}{Z_{om}}\right] \ln\left[\frac{Z_h - d}{Z_{oh}}\right]}{k^2 U_z}, \quad (12)$$

where  $Z_m$  is the wind measurement height (m), 2 m,  $Z_h$  is the humidity measurement height (m), 2 m,  $d$  is the zero plane displacement height, 0 m,  $Z_{om}$  is the roughness length governing momentum transfer (m),  $Z_{oh}$  is the roughness length governing the transfer of heat and vapour

(m),  $k$  is the von Karman constant, 0.4 (–) and  $U_z$  is the wind speed at height  $z$  ( $\text{m s}^{-1}$ ).

When calculating the  $r_d$  of the roof and the ground separately, the value of  $Z_{\text{om}}$  of the roof is taken as 0.01 m and  $Z_{\text{om}}$  of the ground is taken as 0.003 m (Meili et al., 2020). The albedo is 0.2, which applies to urban areas (Li et al., 2016), and some impervious materials, such as roofs, roads and walls. Impervious surfaces have a certain water-storage capacity. Referring to the research of Zhou et al. (2021), using the design requirements of sponge cities, the maximum water depth is set at 2 mm.

Roof PET ( $\text{mm day}^{-1}$ ):

$$\text{PET}_{\text{Roof}} = \frac{0.408\Delta(R_n - G)}{\Delta + \gamma} + \frac{\gamma \frac{736}{T+273} U_{Z_{\text{rooftop,ref}}} (e_s - e_a)}{\Delta + \gamma}. \quad (13)$$

GH PET ( $\text{mm day}^{-1}$ ):

$$\text{PET}_{\text{GH}} = \frac{0.408\Delta(R_n - G)}{\Delta + \gamma} + \frac{\gamma \frac{518}{T+273} U_{Z_{\text{ground,ref}}} (e_s - e_a)}{\Delta + \gamma}. \quad (14)$$

GO PET ( $\text{mm day}^{-1}$ ):

$$\text{PET}_{\text{GO}} = \frac{0.408\Delta(R_n - G)}{\Delta + \gamma} + \frac{\gamma \frac{518}{T+273} U_2 (e_s - e_a)}{\Delta + \gamma}, \quad (15)$$

$$D = \begin{cases} H_0, & P_d \geq H_0 \\ P_d, & P_d < H_0 \end{cases}, \quad (16, 17)$$

$$E = \begin{cases} D, & \text{PET} \geq D \\ \text{PET}, & \text{PET} < D \end{cases} \quad (18, 19)$$

where  $D$  is the water depth intercepted by impervious surfaces (mm),  $H_0$  is the maximum water depth intercepted by impervious surfaces (mm),  $P_d$  is the precipitation in 1 day (mm) and  $E$  is the impervious surface evaporation (mm).

If the PET of the day is insufficient to evaporate water from the impervious surface, part of the intercepted water remains until the next day for further evaporation.  $H_0$  is replaced with 2 mm in Equations (20) and (21). Figure 2 illustrates this process.

$$D_2 = \begin{cases} D_{\text{rest1}} + P_2, & D_{\text{rest1}} + P_2 < 2 \\ 2, & D_{\text{rest1}} + P_2 \geq 2 \end{cases} \quad (20, 21)$$

$$E_2 = \begin{cases} D_2, & \text{PET}_2 \geq D_2 \\ \text{PET}_2, & \text{PET}_2 < D_2 \end{cases} \quad (22, 23)$$

where  $D_2$  is the water depth intercepted by impervious surfaces on the second day (mm) and  $D_{\text{rest1}}$  is the remaining water depth until the second day on the impervious surfaces (mm).  $P_2$  is the precipitation on the second day (mm).  $P_2 \geq 0$  and  $E_2$  is the impervious surface evaporation on the second day (mm).

### 2.3.3 | Dividing the precipitation year type

This study refers to the ‘Norms for Hydrological Information Forecasting’ and used the anomalous percentage to divide the annual precipitation into wet and dry year (DY) types. The classification results are shown in Table 1.

$$\omega = \frac{\text{PRP}_{\text{BYD}} - \text{PRP}_{\text{ave}}}{\text{PRP}_{\text{ave}}} \times 100\%, \quad (24)$$

where  $\omega$  is the anomalous percentage of annual precipitation,  $\text{PRP}_{\text{BYD}}$  is the annual precipitation in the BYD (mm) and  $\text{PRP}_{\text{ave}}$  is the average annual precipitation in the BYD from 1980 to 2020 (mm).

### 2.3.4 | Impervious surface area fraction

The impervious surface area fraction (IF), also known as the Impervious Surface Index (Kuang et al., 2013), refers to the fraction of the impervious surface in  $250 \text{ m} \times 250 \text{ m}$  grids, ranging from 0% to 100%.

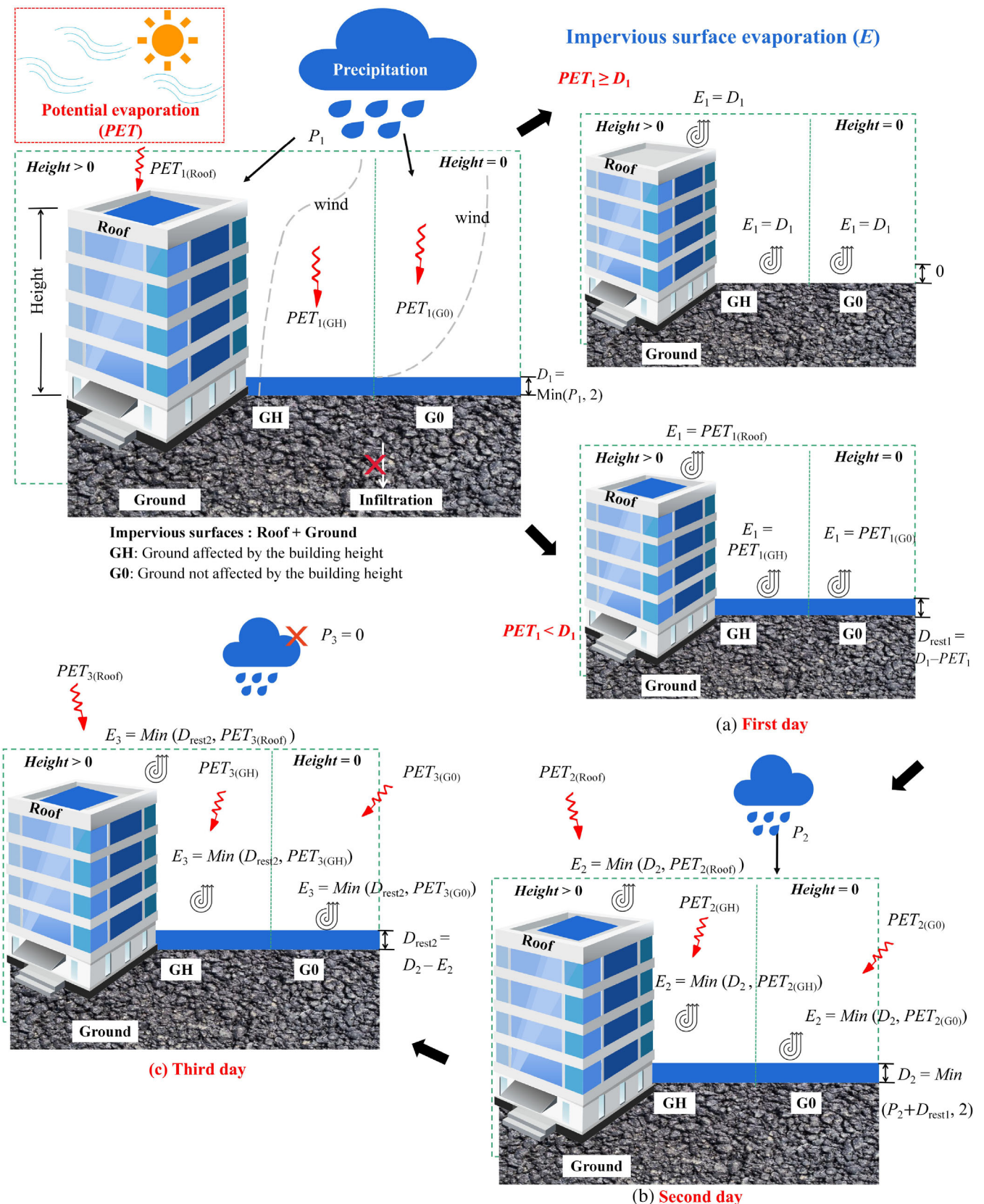
$$\text{IF} = \frac{\text{impervious surface area in each grid}}{\text{gridsize}} \times 100\%, \quad (25)$$

where gridsize represents  $250 \times 250 (\text{m}^2)$ .

It was necessary to calculate the amount of water consumed by evaporation, which requires an impervious surface area. For the CLCD data of the long time series from 1985 and 1990 to 2020, when studied on a 30 or 5 m scale (Figure 3), the impervious surface range could not be revised. The BYD comprises a relatively large area. If it is calculated at a resolution of 5 m, the number of grid points would be too large, and the computer would not have sufficient computing power. For the HR data with a resolution of 5 m in 2020 and the CLCD data with a resolution of 30 m, the proportions of the impervious surface area in the catchment were 11.6% and 15.3%, respectively. After converting these into area fraction data, the proportions of impervious surface area in the catchment area were similar, that is, 11.9% and 15.2%, respectively. The main revision steps are illustrated in Figure 4.

### 2.3.5 | Revised CLCD data

The impervious surface area of the BYD (Figure 5) from 1985 to 2020 exhibited a significant increasing trend ( $p < 0.001$ ). Before revision, the impervious surface area increased from  $2.2 \times 10^9 \text{ m}^2$  to  $5.4 \times 10^9 \text{ m}^2$ , and the proportion increased from 6.2% to 15.2%, with a growth rate of  $2.7 \times 10^{-3}$  ( $p < 0.001$ ). The revised area increased from  $1.88 \times 10^9 \text{ m}^2$  to  $4.41 \times 10^9 \text{ m}^2$ , accounting for an increase in the proportion of catchment area from 5.3% to 12.4%, with a rate of increase of  $2.1 \times 10^{-3}$  ( $p < 0.001$ ). The impervious surface area before and after revision changed similarly annually, indicating that

**FIGURE 2** Legend on next page.

**TABLE 1** Classification of precipitation year types.

Precipitation year type	Year							
DY	1997	1984	2001	1999	2006	2014	1993	
DEY	2000	1986	2005	2009	2002	1989	2019	
NY	1983	2010	1980	1998	1981	1992	2018	2007
	2003	2017	2004	1987	2015	2020	1982	2011
WEY	2013	2016	2012					
WY	2008	1991	1995	1996	1994	1990	1985	1988

Note:  $\omega$  is the anomalous percentage of annual precipitation,  $\omega > 20\%$  is the wet year (WY);  $10\% < \omega \leq 20\%$  is the wetter year (WEY);  $-10\% \leq \omega \leq 10\%$  is the normal year (NY);  $-20\% \leq \omega < -10\%$  is the drier year (DEY); and  $\omega < -20\%$  is the dry year (DY).

the revision is in line with urban development trends. In 1985, the northeast of the BYD and the central area of the plain region had a significantly high impermeability ratio, including Fangshan in Beijing and Baoding. The other areas with an area score of 80%–100% were residential villages distributed in a dotted pattern. By 2020, there were significant changes in these areas with an area fraction between 80% and 100%, as shown by an increase in distribution. The increase in connections between villages was mainly because of road construction. The changes in the mountainous areas of the BYD were also prominent. This reflected increased distributions of impervious surfaces and the fractions of the impervious surface area. The rapid expansion of impervious surfaces reflected the accelerating urbanization process, which increased the complexity of hydrological processes.

### 2.3.6 | Long time series of roof area fraction data

The method described in Section 2.3.4 was used to convert the roof data (building roofs in HR) in Section 2.2.1 in 2020 to the roof area fraction (RAF). The RAF in 2020 was subtracted from the revised IF in 2020, and the result was named the ‘area fraction difference’. For grid points where the area fraction difference was greater than zero, the RAF remained unchanged. For grid points where the area fraction difference was less than zero, the RAF was replaced by the corresponding IF.

The new 2020 RAF was divided by 2020 IF to obtain the ‘ratio’. This ratio was then multiplied by the IF for each year to obtain the RAF for each year. Given that the data sources of the building height data and the roof data are different, there are situations where height  $> 0$

but RAF = 0. The grid points where height  $> 0$  were extracted when RAF = 0 and replaced with the corresponding IF values to obtain the annual RAF. The difference between the 2020 roof area obtained using this method and the original roof area was 5%. The difference between IF and RAF was considered as the fraction of the ground.

### 2.3.7 | Water consumption rate of impervious surface evaporation

$$EA = \sum_{1}^{\text{day}} E \times IF \times \text{gridsize}, \quad (26)$$

$$PA = \sum_{1}^{\text{day}} P_d \times \text{gridsize}, \quad (27)$$

$$DRY = \frac{\sum_{1}^i EA}{\sum_{1}^i PA} = \frac{EAP}{PAP}, \quad (28)$$

where EA represents the amount of water consumed by impervious surface evaporation (kg). PA represents the amount of water provided by precipitation in grid points containing impervious surfaces with a grid data resolution of 250 m (kg). DRY represents the proportion of impervious surface evaporation to precipitation. day represents all the days of the year or month.  $i$  represents the number of impervious surface grid points in the area fraction data. EAP represents the cumulative amount of water consumption by evaporation for all the grid points containing impervious surfaces on a yearly or monthly scale (kg). PAP represents the cumulative precipitation of all the grids containing impervious surfaces on a yearly or monthly scale (kg).

**FIGURE 2** Schematic diagram of the research method presented in the current study. Impervious water surface including roof and ground, where the ground is divided into ground affected by the building height (GH) and ground not affected by the building height (G0). On the first day, the precipitation is  $P_1$ , and the interception depth of impervious surfaces is  $D_1$ .  $D_1 = \text{Min}(P_1, 2)$ . The roof, GH, and G0 undergo evaporation processes, respectively. If the potential evaporation  $PET_1 \geq D_1$ , the interception depth  $D_1$  will evaporate completely. At this point, the evaporation from impervious surfaces  $E_1$  is equal to the interception depth  $D_1$ . If the  $PET_1 < D_1$ , a portion of the precipitation is retained until the next day, and the remained water depth  $D_{\text{rest}1} = D_1 - PET_1$ . The  $E_1$  is equal to  $PET_1$ . If there is precipitation  $P_2$  on the second day, the interception depth of impervious surfaces on the second day is  $D_2 = \text{Min}(P_2 + D_{\text{rest}1}, 2)$ . The roof, GH, and G0 undergo the evaporation process. The evaporation is the smaller value of the interception depth  $D_2$  and the potential evaporation  $PET_2$ . If there is water remaining and no precipitation on the third day, the evaporation process will continue.

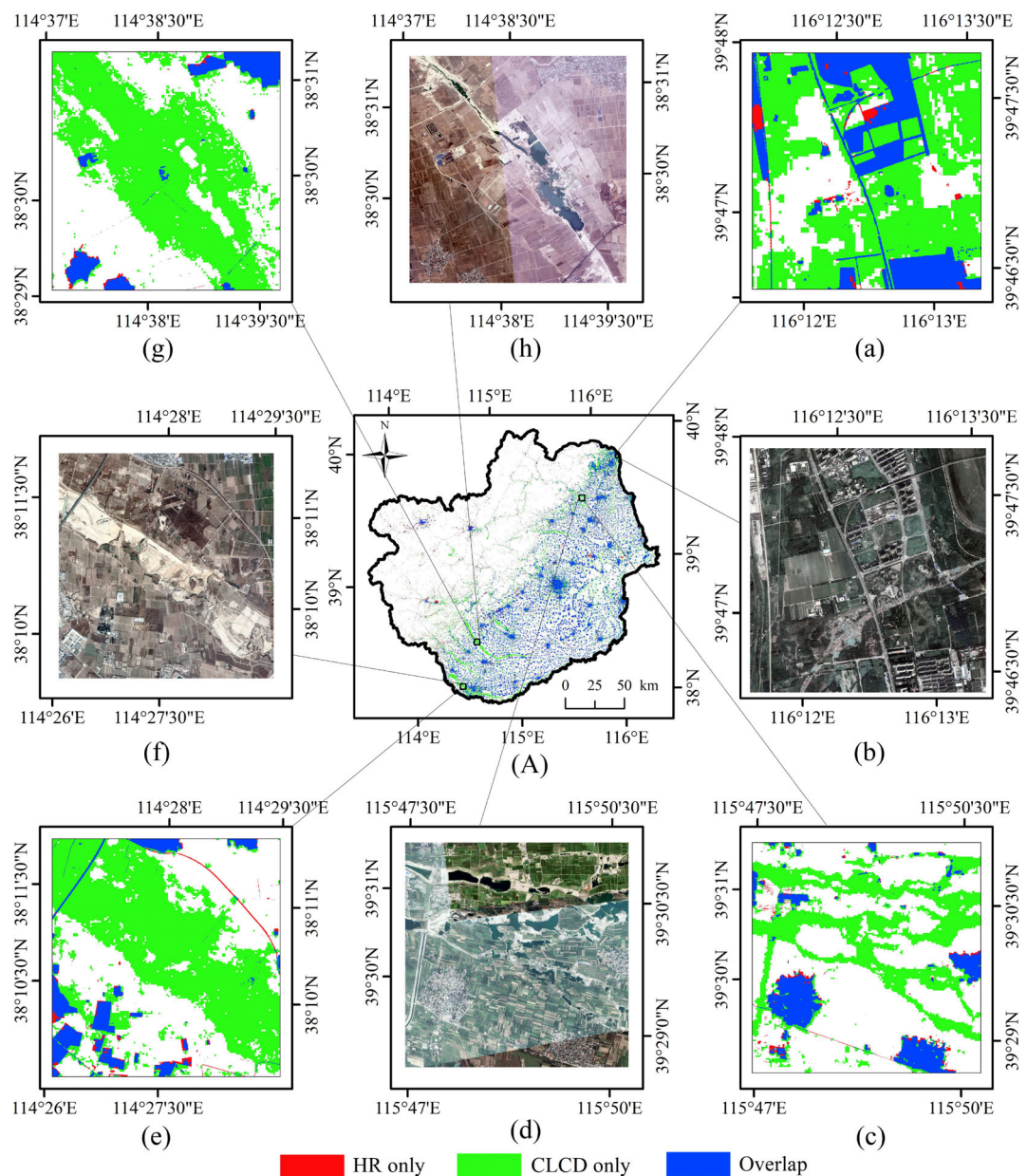


**FIGURE 3** Local comparison chart of CLCD and HR. Resampling the 2020 CLCD data to 5 m and overlaying it with the 2020 HR data (A). The blue parts represent the areas where the two sets of data overlap. The red part only represents HR, and the green part only represents CLCD. The CLCD and HR data overlap in most regions. However, there are still some incorrect classifications in the CLCD data. The CLCD data identifies riverbanks and vegetation as impervious surfaces, such as (a), (c), (e) and (g). This corresponds to the actual images of (b), (d), (f) and (h). The land use type ‘impervious’ extracted from the China land cover dataset is expressed as CLCD. HR represents high-resolution impervious data.

### 2.3.8 | Statistical methods

The main statistical method used in this article is linear regression analysis. In the multiple regression equation, the absolute values of the standardized coefficients of each independent variable are taken. They are then divided by the sum of them to obtain the contribution of each independent variable. Pearson correlation is used to test the correlation between variables, and the magnitude of the correlation is represented by the correlation coefficient  $r$ . The  $p$ -value is used to verify whether the results are significant. If  $p < 0.05$ , the correlation between the variables is considered

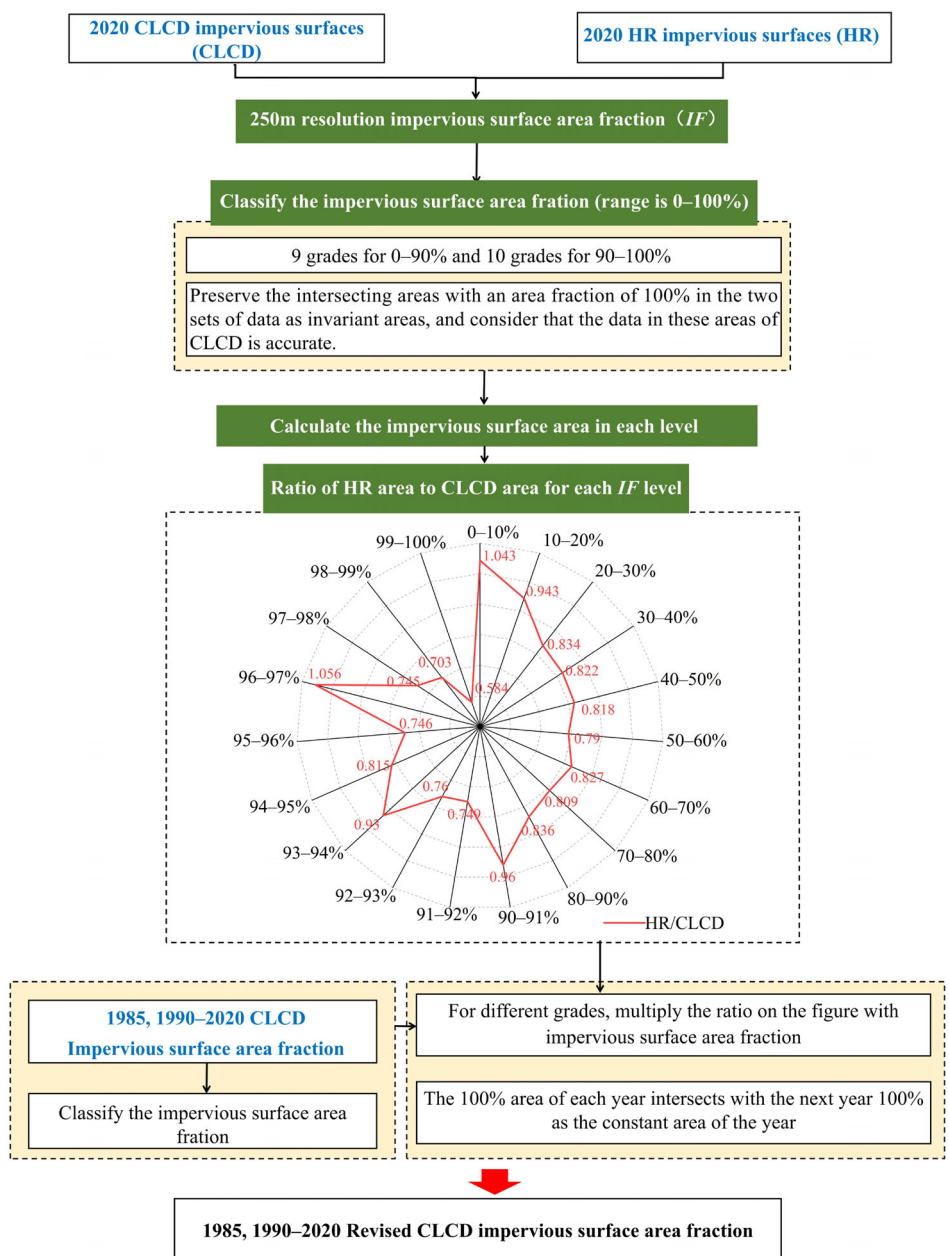
significant. If  $p < 0.001$ , the results are considered highly significant.

## 3 | RESULTS

### 3.1 | Spatial and temporal distribution pattern and trend analysis

The spatial distributions of the total annual precipitation in grid points containing impervious surfaces ( $\text{PRP}_y$ ), potential evaporation  $\text{PET}_y$ ,

**FIGURE 4** Revision steps for CLCD. In most ranges, the two sets of data maintain a ratio of approximately 0.8. This is consistent with the area ratio of HR to CLCD at the entire catchment scale. There is an obvious difference between the two sets of data at some levels, which is related to the misclassification of the CLCD data.



( $\text{PET}_{\text{Roof},y}$ ,  $\text{PET}_{\text{GH},y}$ ,  $\text{PET}_{\text{GO},y}$ ), and impervious surface evaporation  $E_y$  ( $E_{\text{Roof},y}$ ,  $E_{\text{GH},y}$ ,  $E_{\text{GO},y}$ ) on impervious surfaces of the BYD were uneven. There were significant differences between the highest and lowest values (Figure 6). The  $\text{PRP}_y$  gradually decreased from west to east. The highest value was 850 mm/year, which was 2.6 times that of the lowest value. The regional average  $\text{PRP}_y$  was 530 mm/year, with 88% of the grid points of  $\text{PRP}_y > 500$  mm/year. The distribution of  $\text{PET}_{\text{Roof},y}$  and  $\text{PET}_{\text{GH},y}$  is higher in the southeast than in the northwest. Meanwhile, the overall distribution of  $\text{PET}_{\text{GO},y}$  is relatively uniform, with low values in the central area of the BYD. The spatial pattern for  $E_y$  was consistent with that of  $\text{PRP}_y$ . This indicates that precipitation in grid points containing impervious surfaces (PRP) was the dominant factor in impervious surface evaporation. In areas with high PRP, impervious surface evaporation was also relatively high.  $E_y$  was

significantly higher in the north-western mountainous area than in the south-eastern plain. The highest value reaches 178.2 mm/year (Figure 6f). Shao et al. (2022) found that the ratio of impervious surface evaporation to vegetation surface ET was 1:4.1. Based on the PML\_V2 product research, Mushimiyama et al. (2023) showed that the average ET in the BYD from 2002 to 2018 was 541.2 mm. Combined with the results of this study, the ratio of  $E_y$  to ET was approximately 1:5, which is slightly lower than 1:4.1. This is because impervious surface evaporation was not considered separately by Mushimiyama. In that study, impervious surface evaporation was estimated in the same way as other natural surfaces—resulting in evaporation from the impervious surface as high as 400–500 mm/year—which overestimated the ET of the study area. The results have demonstrated the importance of evaporation from impervious

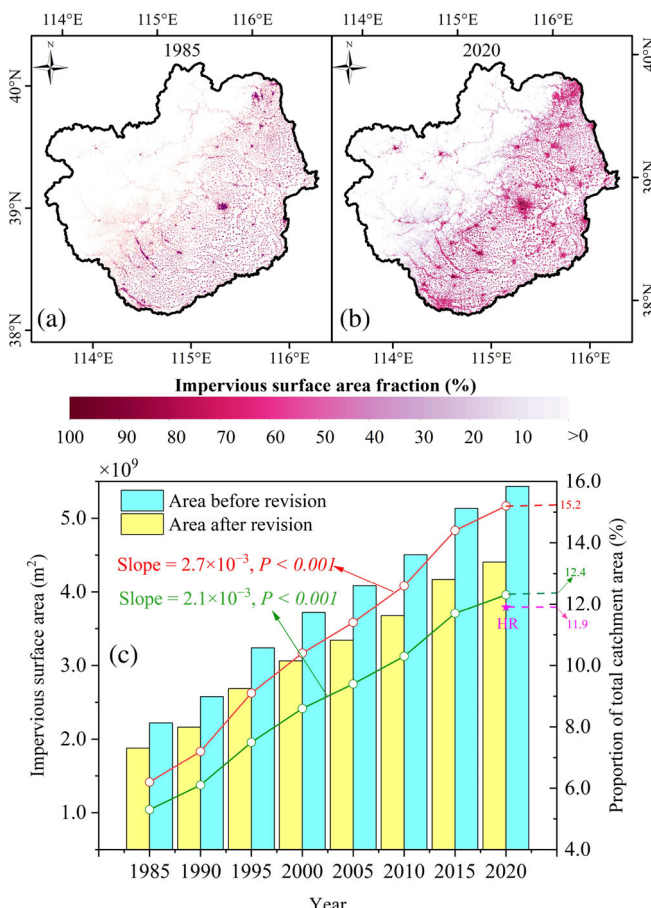


**FIGURE 5** Impervious surface area fractions of the BYD in (a) 1985 and (b) 2020. Area of the BYD from 1985 to 2020 before and after revision (c). In (a) and (b), blank areas indicate that there are no impervious surfaces. In (c), the red line represents the change in the proportion of the impervious surface area to the total area of the catchment before revision. The growth rate of this ratio over time is  $2.7 \times 10^{-3}$  ( $p < 0.001$ ). The green line represents the change in the proportion of the impervious surface area to the total catchment area after revision. The growth rate of this ratio over time is  $2.1 \times 10^{-3}$  ( $p < 0.001$ ). The five-pointed star represents the proportion of HR with 5 m resolution in 2020 to the catchment area with a value of 11.9.

surfaces and have highlighted the need to focus on changes in urban water from changes in land cover.

After considering their impervious surface area, the distribution of evaporated water from impervious surfaces (EA) has a different distribution (Figure 6h). High values occurred in high IF areas, such as the urban area of Baoding. Meanwhile, in the high IF area, EA/PA is also higher (Figure 6i), with the highest value reaching 0.28. In some low IF areas, such as the southwestern mountainous area, the EA/PA ratio was relatively small, with 17.3% of the grid points of EA/PA greater than 0.1. The higher the IF, the more PRP fell on the impervious surface area in the precipitation distribution area. All the PRP intercepted by impervious surfaces enters the evaporation process, which affects the regional water cycle and microclimate. Therefore,

hydrological research in urban areas needs to focus on the impact of impervious surface evaporation on the climate, urban water use structure, and timely allocation of water.

From 1980 to 2020, the BYD received a large number of water resources via precipitation. In the impervious surface area, the cumulative precipitation of all grids containing impervious surfaces (PAP) per year was between  $3.85 \times 10^{12}$  and  $9.10 \times 10^{12}$  kg. The cumulative amount of water evaporated from the impervious surface (EAP) was between  $1.79 \times 10^{11}$  and  $5.12 \times 10^{11}$  kg. Although there is no prominent trend in the temporal changes in PRP, with the expansion of the impervious surface (Figure 5), EAP showed a significant upward trend, with a rate of  $6.68 \times 10^9$  ( $p < 0.001$ ). The annual rate of change in EAP since 1980 was 0.03 ( $p < 0.001$ ), as shown by the blue line graph in Figure 7b. Compared with that in 1980, in 2020, EAP increased by 134.4%. The ratio of EAP to PAP (DRY<sub>y</sub>) ranged from 3.0% to 6.9%. It significantly increased in a fluctuating manner ( $p < 0.001$ ). The lowest value occurred in 1985, and the highest value occurred in 2006. The annual average value of DRY<sub>y</sub> was 5.16%.

### 3.2 | The impacts of precipitation year type on impervious surface evaporation

According to the different precipitation year types shown in Table 1, statistics were calculated on the average values of PAP (PAP<sub>ave</sub>), EAP (EAP<sub>ave</sub>) and DRY<sub>y</sub> (DRY<sub>ave</sub>). The results are shown in Figure 8. From the DY to the wet year (WY), PAP<sub>ave</sub> and EAP<sub>ave</sub> displayed an upward trend. DRY<sub>ave</sub> showed a strong downward tendency (Figure 8), with  $p < 0.001$ , the DRY<sub>ave</sub> = 6.3% in the DY, and the DRY<sub>ave</sub> = 3.7% in the WY. In the WY and the wetter year (WEY), the pressure on water resources was alleviated. While the WEY occurred after 2010, most of the WYs occurred before 2000. The range of impervious surfaces in the WEY period was larger, so the PAP<sub>ave</sub> in the WEY and WY periods were similar. The PAP<sub>ave</sub> in the WEY was  $2.8 \times 10^{10}$  kg less than that in the WY, but the difference is not apparent in Figure 8.

From DY to WEY, the changing trend of the evaporation of impervious surfaces conformed to the notion that the greater the PRP, the greater the evaporation. However, the EAP<sub>ave</sub> of the WY was significantly lower than that of the WEY. A potential cause of these abnormal results is that the impervious surface can only intercept a maximum depth of 2 mm of water. When the number of precipitation days (PD) was relatively low and the PRP intensity was relatively high, most of the PRP formed runoff that could not be intercepted by impervious surfaces for further evaporation.

The differences in DRY<sub>y</sub> are shown in more detail in Figure 9. In DY, DRY<sub>y</sub> is larger than that in WY, and the colour of DRY<sub>y</sub> is mainly red (Figure 9a). Comparing the two figures in Figure 9 shows that the value of DRY<sub>y</sub> in some years is abnormal compared to the same group, such as 1984, 2008 and 2015. Figure 9b shows that, after 2000, the values of DRY<sub>y</sub> are above the trend line. A correlation test was conducted after normalizing the value of DRY<sub>y</sub> and impervious surface area from 1980 to 2020. The Pearson correlation coefficient

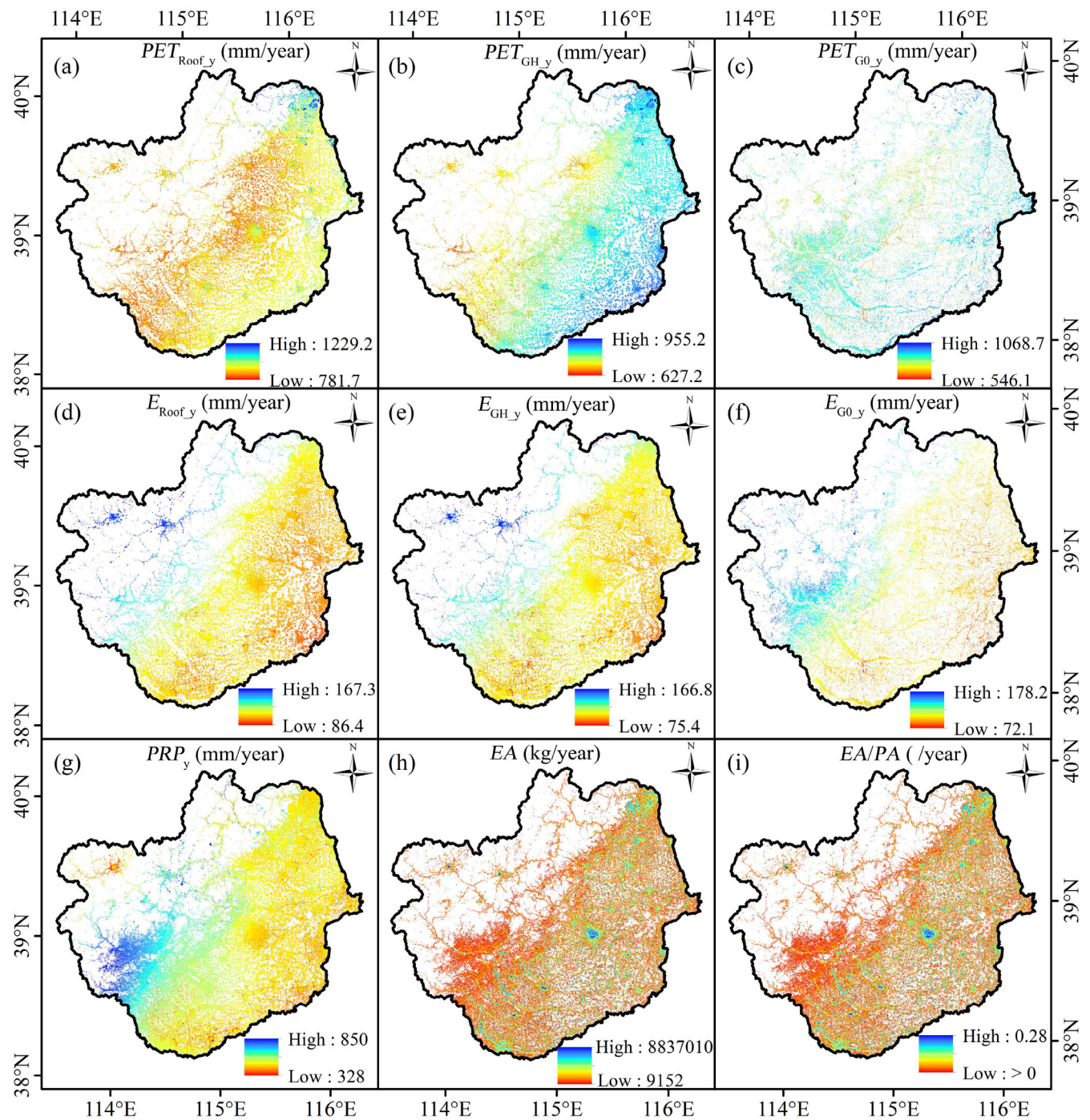


**FIGURE 6** From 1980 to 2020, multi-year average  $PET_y$  for the roof (a), GH (b), G0 (c), multi-year average  $E_y$  for the roof (d), GH (e), G0 (f), annual total precipitation in grid points containing impervious surfaces  $PRP_y$  (g), average annual water evaporation from impervious surfaces EA (h) and the multi-year average ratio of impervious surface evaporation to precipitation EA/PA (i).

$r$  between them was 0.62,  $p < 0.001$ , with a significant positive correlation. The smallest impervious surface area in the same group was recorded in 1984, and 2008 had the largest impervious surface area. The difference in impervious surface area could explain the anomalies in 1984 and 2008 compared to the same precipitation year type. Meanwhile, for 2015, further analysis of influencing factors, such as PD, needed to be conducted.

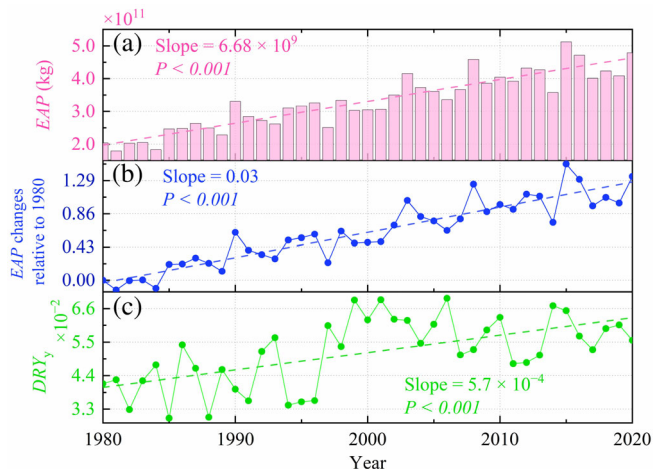
### 3.3 | Effect of precipitation days on impervious surface evaporation

Figure 10a,b show that in the impervious surface region, the average number of PD is 93–201 d/year. Meanwhile, the average number of evaporation days (EA days) is 108–208 d/year. The north-eastern part of the BYD has fewer PD and EA days. For the grid points that pass

the significance test ( $p < 0.05$ ), PD was positively correlated with E for all three impervious surface types (Figure 10c–e). PD and DRY<sub>y</sub> is significantly positively correlated in most areas.

In Figure 8, EAP<sub>ave</sub> does not always increase with PAP<sub>ave</sub>. This means that EAP may be affected by PD. After normalizing PD and EAP<sub>ave</sub>, a correlation between them was established (Figure 11). There is a strong correlation between PD and EAP<sub>ave</sub> ( $p < 0.05$ ). The average

number of PD in WEY is 50 days higher than that in WY. The average PD in NY is 11 days higher than in WY. Meanwhile, the number of days with PRP greater than 2 mm in WEY is generally less than that in WY. The ground maximum interception water depth is 2 mm. Therefore, most of the PRP forms runoff, which is the main reason for the low EAP value in WY. In Figure 9, DRY<sub>y</sub> in 2015 is relatively abnormal in NY. Comparing PD in other years in NY shows that PD in



**FIGURE 7** Change in EAP over time (a), change rate of EAP relative to 1980 (b), change of DRY<sub>y</sub> over time (c). EAP refers to the cumulative amount of water consumption by evaporation of all grid points containing impervious surfaces in a year (kg). PAP refers to the cumulative precipitation of all grids containing impervious surfaces in a year (kg), and DRY<sub>y</sub> refers to the ratio of EAP to PAP on an annual scale.

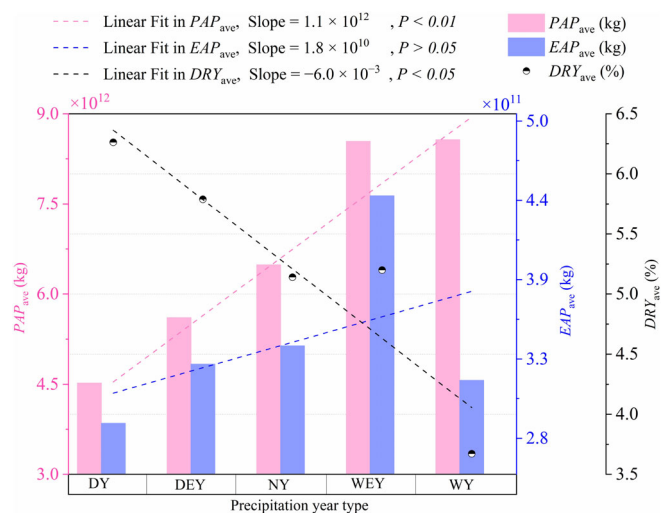


**FIGURE 8** Average values of PAP, EAP and DRY<sub>y</sub> in different precipitation year types. PAP<sub>ave</sub> represents the average value of PAP, EAP<sub>ave</sub> represents the average value of EAP, and DRY<sub>y</sub> represents the average value of DRY<sub>y</sub>. WY is the wet year, WEY is the wetter year, NY is the normal year, DEY is the drier year and DY is the dry year.

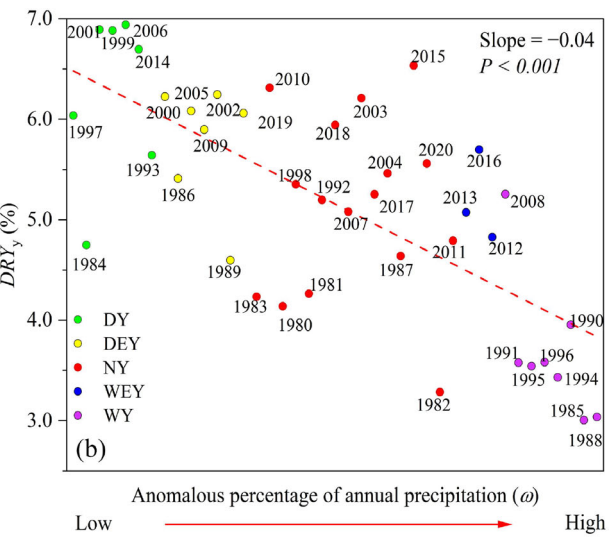
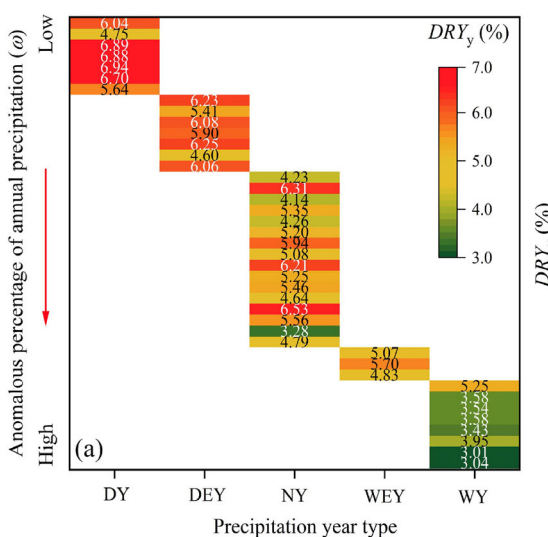
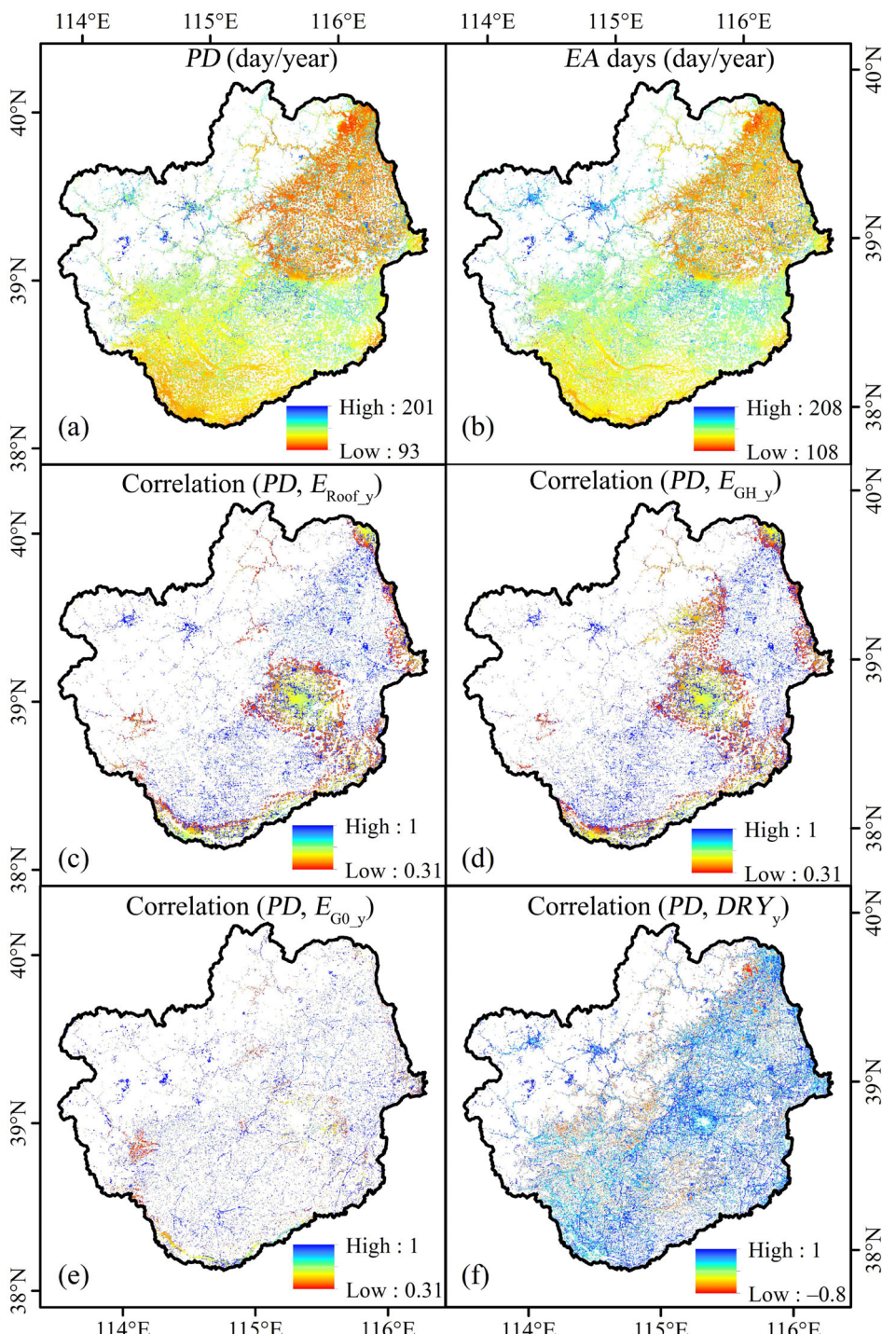


**FIGURE 9** DRY<sub>y</sub> in different precipitation year types (a). DRY<sub>y</sub> changes with the anomalous percentage of annual precipitation (b). In (a), the horizontal axis represents the precipitation year types. The vertical axis is the anomalous percentage of annual precipitation. The vertical axis is the anomalous percentage that goes from low to high from top to bottom. In (b), the horizontal axis is the anomalous percentage of annual precipitation. The horizontal axis goes from low to high from left to right. The vertical axis is the DRY<sub>y</sub> and the color of the point corresponds to different precipitation year types.

**FIGURE 10** Average number of precipitation days (PD) from 1980 to 2020 (a). Average number of evaporation days (EA days) from 1980 to 2020 (b). Correlation coefficient  $r$  between PD and roof evaporation  $E_{\text{Roof},y}$  (c),  $r$  between PD and GH evaporation  $E_{\text{GH},y}$  (d),  $r$  between PD and G0 evaporation  $E_{\text{G0},y}$  (e), and  $r$  between PD and DRY<sub>y</sub> (f). Grid points that pass the significance test at  $p < 0.05$ .



2015 reached 252. This is the highest number in NY, exceeding the average PD in the same group by 50. There were 160 PD in 1984, which was 22 less than the average number of PD in the same group. The number of PD in 2008 was also the highest in the same group (251 days). This was 60 days higher than the average number of PD in the same group. Therefore, the impervious surface area and PD could explain the inconsistent DRY<sub>y</sub> values for these years.

The factors that have a greater impact on  $E$  and related results (EAP, DRY<sub>y</sub>) are PRP, PET, PD and impervious surface area. Given that the total PET is obtained by summing the product of three types of impervious surface area fraction and corresponding PET, PET is not

considered as an independent variable in Table 2 (see Appendix C for details). The effects of PRP and impervious surface area on EAP and DRY<sub>y</sub> were significant. The contribution of impervious surface area to EAP was 71.3%. This means that with the expansion of the impervious surface, EAP can increase rapidly. The contribution of PRP is 20.5%, likely because the influence of PRP is constrained by  $H_0$ . For DRY<sub>y</sub>, the contributions of the impervious surface area and PRP are similar. The increase in impervious surface area can lead to an increase in DRY<sub>y</sub>, which is the same as the results in Figure 9b. The coefficients of PD are relatively small. From 1980 to 2020, there was a strong correlation between the number of PD and impervious surface area ( $r = 0.657$ ,

$p < 0.001$ ). A binary regression equation (Table 3) was developed to avoid the interaction between the two independent variables.

As shown in Table 3, impervious surface area and PD have a strong effect on EAP, while PRP has a prominent effect on  $DRY_y$ . These results are in line with previous findings (Figures 8–10). PD is an important factor for impervious surface evaporation. However, it has often been overlooked in previous studies. An increase in PRP may lead to an increase in evaporation, but to a greater extent, it alleviates water stress.

### 3.4 | Relationship between monthly-scale precipitation and evaporation from impervious surfaces

Monthly analysis of EAP shows that from 1980 to 2020, the average EAP in January, February and December was relatively small, ranging

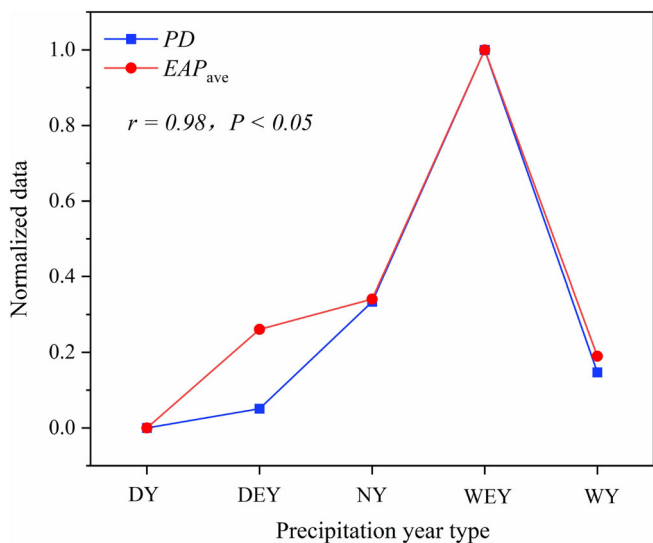


**FIGURE 11** Line graph of PD and  $EAP_{ave}$  in different precipitation year types. PD and  $EAP_{ave}$  in different annual types are normalized. The line graphs of the two are highly similar,  $r = 0.98$ ,  $p < 0.05$ .

Dependent variable	Regression coefficients	Independent variable		
		Impervious surface area	PD	PRP
EAP	Not standardized	0.69*	0.08	0.22*
	Standardized	0.87*	0.1	0.25*
	Contribution	71.3%	8.2%	20.5%
$DRY_y$	Not standardized	0.51*	-0.06	-0.63*
	Standardized	0.59*	-0.06	-0.66*
	Contribution	45.0%	4.6%	50.4%

Note: A regression equation was established with EAP and  $DRY_y$  as dependent variables. PRP, PD and impervious surface area were the independent variables. All the multiple regression equations were statistically significant ( $p < 0.001$ ).

\*Significant coefficient at  $p < 0.001$ .

from  $4.26 \times 10^9$  to  $7.64 \times 10^9$  kg. Meanwhile, the values in other months were higher than  $1.12 \times 10^{10}$  kg, with the highest value at  $7.12 \times 10^{10}$  kg being recorded in July. PAP has the same distribution as EAP.  $DRY_m$  from January to December shows an increasing temporal trend (Figure 12). Among these, the increasing trend of  $DRY_m$  in January, June and August is highly significant ( $p < 0.001$ ), with growth rates of 0.30, 0.13 and 0.07, respectively. The correlation between  $DRY_m$  and the impervious surface area is high in January, June and August, with each  $r$  higher than 0.5 ( $p < 0.001$ ). The increasing trends in May, July, October and December are also significant ( $p < 0.05$ ), and maintained a significant correlation with the impervious surface area ( $p < 0.05$ ). The  $DRY_m$  values from January to March, and November and December, are generally higher than those of other months. There was a multi-year average  $DRY_m$  ranging from 13.2% to 21.2%. The multi-year average  $DRY_m$  in other months ranged from 4.0% to 10.3%. This is because there is less monthly precipitation from January to March, and in November and December.

Although Figure 12 shows that  $DRY_m$  increases with impervious surface expansion and is higher in cold months than in other months, daily PET in cold months may generally be lower than in hot months. When PRP occurs at the end of the month and there is no PRP at the beginning of the next month, evaporation may continue. This causes the evaporation from impervious surfaces each month to be affected by the PRP at the end of the previous month. Although this situation is rare, it needs to be considered and may result in  $DRY_m$  being overestimated.

## 4 | DISCUSSION

### 4.1 | Impacts of parameter settings on results

#### 4.1.1 | Impacts of the 1985 average building height setting

Given the lack of historical data and long time series of building height data, in the method used in the current study, the average building height in 1985 was set to 5 m. Then a linear equation was established

**TABLE 2** Contributions of impervious surface area, precipitation days (PD), and PRP to EAP and  $DRY_y$ , respectively.

**TABLE 3** Contributions of PRP and impervious surface area or PD to EAP and  $DRY_y$ , respectively.

Dependent variable	Regression coefficients	Independent variable		
		Impervious surface area	PD	PRP
EAP	Not standardized	0.74*	\	0.24*
	Standardization	0.94*		0.27*
	Contribution	77.7%		22.3%
	Not standardized	\	0.57*	0.05
	Standardization		0.70*	0.06
	Contribution		92.1%	7.9%
$DRY_y$	Not standardized	0.47*	\	-0.64*
	Standardization	0.54*		-0.68*
	Contribution	44.3%		55.7%
	Not standardized	\	0.30*	-0.75*
	Standardization		0.34*	-0.79*
	Contribution		30.1%	69.9%

Note: All the multiple regression equations were statistically significant ( $p < 0.001$ ).

\*Significant coefficient at  $p < 0.001$ .

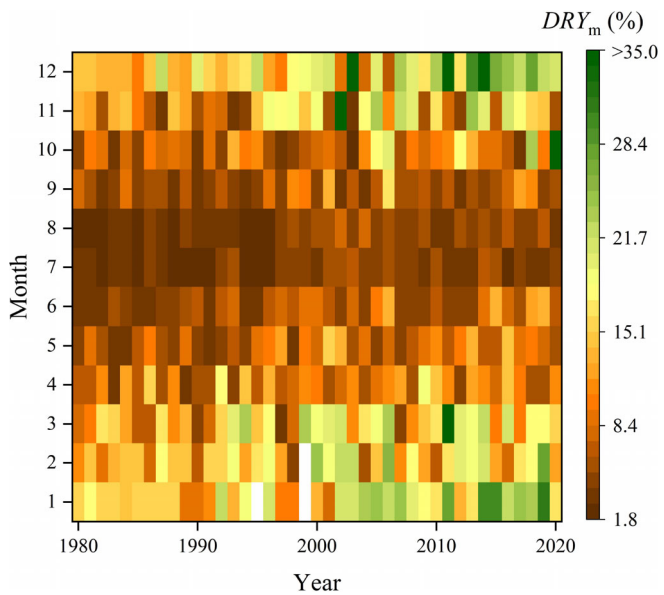


**FIGURE 12**  $DRY_m$  values for each month in 1980–2020. The three white squares in the figure indicate that there was neither PRP nor evaporation from impervious surfaces during that month.  $DRY_m$  refers to the ratio of EAP to PAP on a monthly scale.

and the average building height from 1990 to 2019 was predicted. However, in rural areas with underdeveloped economies in 1985, the average building height was likely to be smaller than 5 m. Therefore, to analyse the effects of the building height settings, the average height of buildings in 1985 was set to 3 m and then calculated.

Figure 13 shows that the average building height in 1985 set to 3 m and 5 m had little effect on the results of EAP. The difference between  $EAP_{5m}$  and  $EAP_{3m}$  becomes smaller over time. The difference was the smallest in 2019, which was  $3.64 \times 10^6$  kg, accounting for 0.01% of  $EAP_{5m}$ . The difference was the largest in 1990, which was  $8.24 \times 10^8$  kg, accounting for 0.25% of  $EAP_{5m}$ .

The building height is important data for PET calculation. The influence of building height cannot be excluded when calculating evaporation from impervious surfaces. Long-term series and high precision building height data can help researchers to improve their understanding of evaporation from impervious surfaces.

#### 4.1.2 | Effect of the maximum water interception depth

There is no accurate or uniform setting for  $H_0$ , and its setting range is mainly between 0.5 and 2 mm (Chen et al., 2023; Ramamurthy & Bou-Zeid, 2014; Willuweit & O'Sullivan, 2013; Zhou et al., 2021). Based on previous experiments and Chinese design specifications,  $H_0$  was set to 2 mm (Zhou et al., 2021). To analyse the impact of  $H_0$  on the evaporation from impervious surfaces,  $H_0$  was set to 0.5, 1 and 1.5 mm, respectively. The same analysis as above was performed on the data from 2020. The results are shown in Figure 14.

The different settings for  $H_0$  have little impact on the spatial distribution of EA but have a considerable impact on the value of EA (Figure 14a–d). Figure 14e–h show the ratio between EA corresponding to different  $H_0$ . Figure 14 shows that the changes in EA are closely related to the changes in the  $H_0$  setting. When  $H_0$  is set to 1 and 0.5 mm, the ratio between the corresponding EA is close to 2 (1.63–1.84) (Figure 14e). This is the same when  $H_0$  is set to 2 and 1.5 mm and the ratio is close to 1.33 (1.19–1.27).

Daily evaporation is jointly constrained by  $H_0$ , PET and PRP on the day. EAP is directly related to the impervious surface area. Due to the use of the 2020 data for this part of the calculations, the effects of building height and impervious surface area are excluded. These results have demonstrated that the  $H_0$  setting has a greater impact on the evaporation from impervious surfaces. When the  $H_0$  range is 0.5–10 mm (Figure 15), EAP has a significant increasing trend with the increase in  $H_0$  ( $p < 0.001$ ). The higher  $H_0$  is set, the more PRP is

intercepted by impervious surfaces. If the daily precipitation in summer is relatively large, and the PET in summer is relatively high, even if 10 mm is intercepted, it may evaporate on the same day. Therefore, the increase of  $H_0$  increases the influence of PRP and PET on evaporation from impervious surfaces. The evaporation from impervious

surfaces does not increase continuously with the increase in  $H_0$ . When the daily PRP and  $H_0$  are both greater than PET, the evaporation from impervious surfaces depends on the PET that day.

## 4.2 | Importance of precipitation iterations

Owing to the physical properties of impervious surfaces, no evaporation occurs if there is no PRP. To date, most studies have used a relatively simple treatment method for impervious surface evaporation (Willuweit & O'Sullivan, 2013), without considering the remaining intercepted water on impervious surfaces. Ramamurthy and Bou-Zeid (2014) confirmed that impervious surface evaporation reaches a peak value and gradually decreases 1–2 days after rain. Impervious surface evaporation continues thereafter.

The current study has used an iterative method to examine the evaporation of remaining water. The PRP intercepted by impervious surfaces on the first day did not completely evaporate. Regardless of whether there has been subsequent PRP, the remaining water continues to evaporate. Section 4.1.2 shows that the setting of  $H_0$  has a significant impact on the results. PET was relatively low during certain periods and was less than the intercepted PRP. To explore the importance of the iterative method, taking the  $\text{PET}_{\text{Roof}}$  as an example, the number of days when  $\text{PET}_{\text{Roof}} < 0.5 \text{ mm}$  was counted from 1980 to 2020. Among them, the number of days when  $\text{PET}_{\text{Roof}} < 0.5 \text{ mm}$  has reached up to 85 days in some regions, mainly concentrated in January, February, November and December.

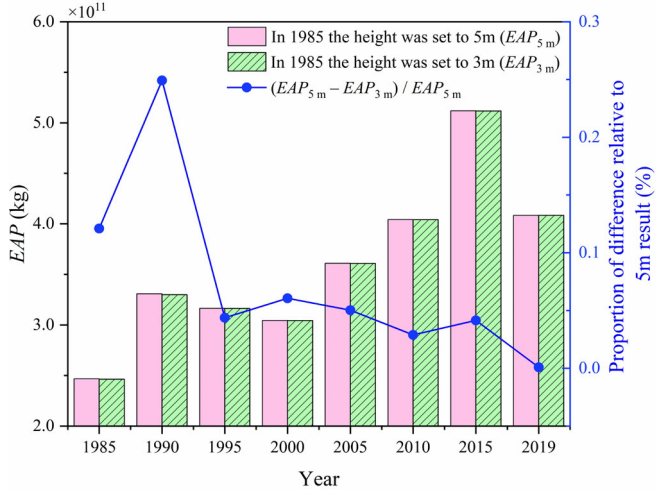


**FIGURE 13** The impact of different building heights on EAP. The red bar shows the EAP (abbreviated as EAP<sub>5m</sub>) when the average building height for 1985 was set to 5 m. The green bar with slashes shows the EAP (abbreviated as EAP<sub>3m</sub>) when the average building height for 1985 was set to 3 m. The line chart is the ratio of the difference between EAP<sub>5m</sub> and EAP<sub>3m</sub> to EAP<sub>5m</sub>.

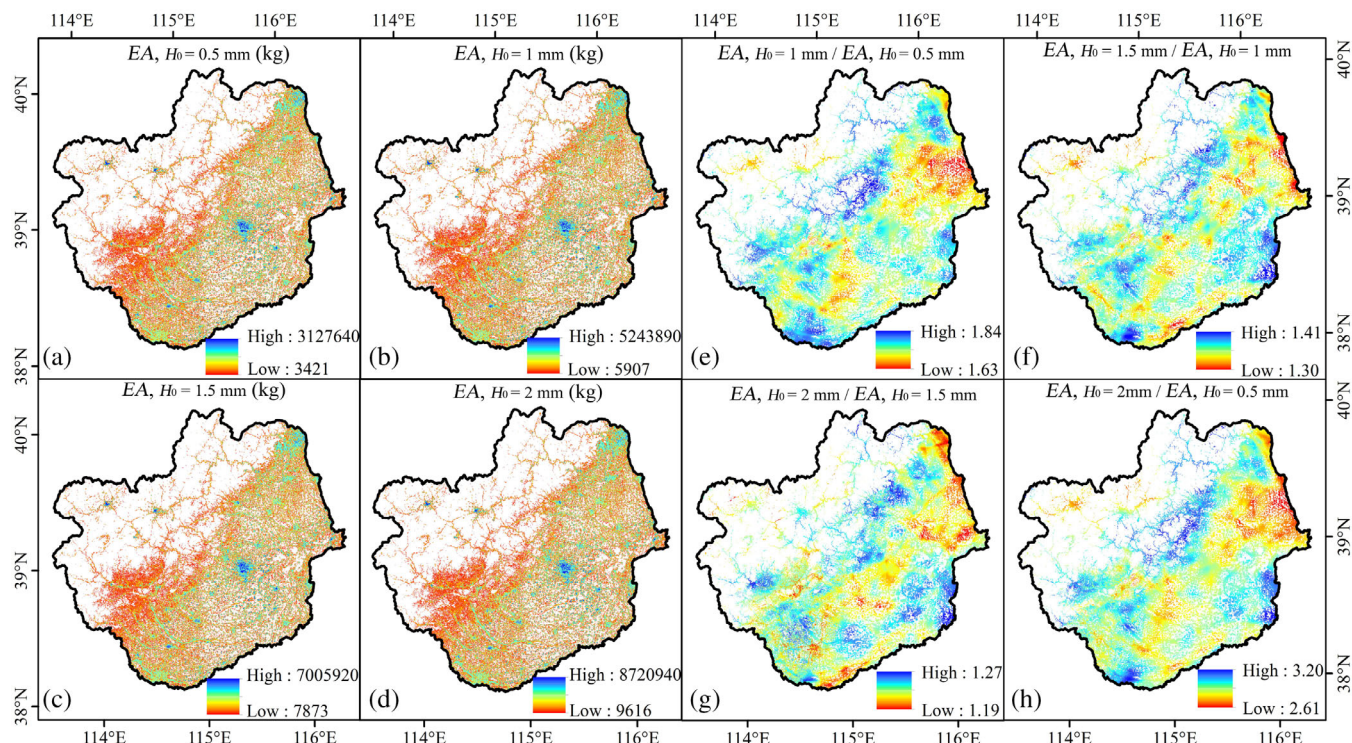


**FIGURE 14** EA corresponding to different maximum water interception depth  $H_0$  in 2020. (a)  $H_0 = 0.5 \text{ mm}$ , (b)  $H_0 = 1 \text{ mm}$ , (c)  $H_0 = 1.5 \text{ mm}$ , (d)  $H_0 = 2 \text{ mm}$ . The ratio between EA corresponding to different  $H_0$  (e), (f), (g) and (h).

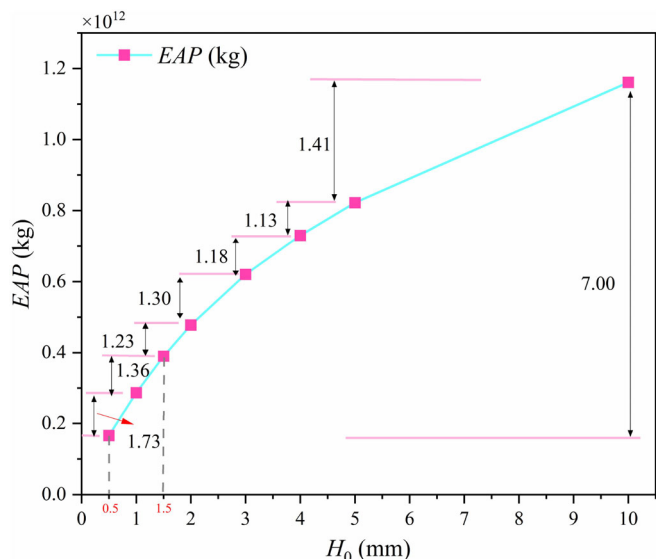


**FIGURE 15** EAP corresponding to different  $H_0$  in 2020. After setting  $H_0$  to 0.5, 1, 1.5, 2, 3, 4, 5 and 10 mm, the changes in EAP (2020) are shown in the figure. The number next to the arrow in the figure represents the proportion between the adjacent two EAP values.

If the influence of iteration was not considered,  $H_0$  was set to 0.5 and 2 mm, respectively. The evaporation of impervious surfaces was calculated using the data from 2020. Comparing EAP showed that when iteration is considered,  $EAP(H_0 = 2\text{ mm}) = 4.79 \times 10^{11}\text{ kg}$ ,  $EAP(H_0 = 0.5\text{ mm}) = 1.66 \times 10^{11}\text{ kg}$ . Without considering iteration,  $EAP(H_0 = 2\text{ mm}) = 4.41 \times 10^{11}\text{ kg}$ ,  $EAP(H_0 = 0.5\text{ mm}) = 1.65 \times 10^{11}\text{ kg}$ . The differences were  $3.75 \times 10^{10}\text{ kg}$  and  $4.91 \times 10^8\text{ kg}$ , respectively. Olympic standard swimming pools generally hold  $2.5 \times 10^6\text{ kg}$  of water, and the difference is approximately 14 998 and 196 swimming pools. Therefore, even if  $H_0$  is 0.5 mm, excluding iteration results in an underestimate of the evaporation from impervious surfaces.

Considering the iteration process implies that the surface runoff has been estimated more accurately. When there is residual water on the day and PRP occurs the next day, the residual water depth of the day should be considered. Therefore, the surface runoff may increase, emphasizing the influence of impervious surface evaporation on the impervious surface confluence process. The relationship between impervious surfaces and runoff has been widely demonstrated (Dams et al., 2013; Kokkonen et al., 2018; Omidvar et al., 2018; Sunde et al., 2018; Zhang et al., 2018; Zhou et al., 2013). This study suggests that the impact of impervious surface expansion on water flow can be estimated more accurately from the perspective of impervious surface evaporation.

### 4.3 | Research limitations and ways forward

Based on previous experiments and monitoring results, this study has optimized the current impervious surface evaporation method. The optimized calculation method is relatively simple and suitable for

long-term analysis of large-scale catchments. However, when the model sets the water storage properties of impervious surfaces, it assumes that all impervious surfaces in the catchment are flat and uniform and have the same water-storage capacity. Owing to the complex topography and construction conditions, the impervious surface is not even. If the surface drainage system is poor or the ground surface has sunk, it is easy to produce deep water and potholes (Mansell & Rollet, 2009; Wouters et al., 2015), making the process of impervious surface evaporation more complex.

## 5 | CONCLUSIONS

The rapid expansion of impervious surfaces has led to complex hydrological processes. Analysing the temporal and spatial distribution of impervious surface evaporation, its corresponding relationship with PRP, and other influencing factors can improve our understanding of urban eco-hydrological processes and the water cycle processes of catchments. In this study, a deep learning method was used to identify impervious surfaces in high-resolution remote sensing images. The high-resolution impervious surface data and 30 m resolution CLCD data were converted into 250 m resolution impervious surface area fractions. Subsequently, CLCD data were revised using high-resolution impervious surface data. The building height was used to distinguish the wind speed on the three types of impervious surfaces, including the roof and the ground affected by or not affected by the building height. PET was calculated according to the modified Penman-Monteith formula, considering the water-storage capacity of impervious surfaces and the daily precipitation to estimate evaporation from impervious surfaces in the BYD. An iterative approach was used to handle the remaining intercepted water until the impervious surface was dry.

From 1980 to 2020, the proportion of impervious areas in the BYD increased from 5.3% to 12.4%. This indicates an increase in the distribution of impervious surfaces and the proportion of impervious surface area. The spatial distribution of PRP<sub>y</sub> varied significantly, with high values in the west and low values in the east, and a multi-year average of 328–850 mm/year. The distribution of evaporation from impervious surfaces was similar to the distribution of PRP. Limited by  $H_0$ , the range of roof evaporation was 86.4–167.3 mm/year, the range of ground evaporation affected by the building height was 75.4–166.8 mm/year, and the range of ground evaporation not affected by the building height was 72.1–178.2 mm/year. The highest and lowest values occurred in the northwest and southeast of the catchment, respectively. EAP showed a significant upward trend, slope =  $6.68 \times 10^9$ ,  $p < 0.001$ , and DRY<sub>y</sub> increased in a zigzag manner over time ( $p < 0.001$ ), with a multi-year average of 5.16%. The DRY<sub>y</sub> value showed a strong downward trend from DY to WY, slope =  $-6.0 \times 10^{-3}$ ,  $p < 0.05$ . PRP was not the only factor affecting evaporation from impervious surfaces. There was a significant positive correlation between EAP and PD in different precipitation year types ( $r = 0.98$ ,  $p < 0.05$ ). PRP, PD, impervious surface area, potential evaporation and water-storage capacity of impervious surfaces all had a

non-negligible effect on impervious surface evaporation. Impervious surface evaporation in the BYD changed the water cycle process in the catchment. In drought years, it is particularly important to pay attention to the hydrological process of impervious surfaces, strategically allocate water resources, handle surface drainage, focus on drought and flood disasters, and consider the balance of water use in all contexts.

## ACKNOWLEDGEMENTS

Thanks to the reviewers for their valuable and detailed comments and suggestions, which have enriched the study contents.

## FUNDING INFORMATION

This study was funded by project of National Key Research and Development Program of China (grant nos. 2022YFF0801804, 2018YFE0106500).

## DATA AVAILABILITY STATEMENT

The data that support the findings of this study are available from the corresponding author upon reasonable request.

## ORCID

Xiaoyu Liu  <https://orcid.org/0009-0000-8733-4078>

## REFERENCES

- Ackerman, D., & Stein, E. D. (2008). Estimating the variability and confidence of land use and imperviousness relationships at a regional scale 1. *JAWRA Journal of the American Water Resources Association*, 44(4), 996–1008. <https://doi.org/10.1111/j.1752-1688.2008.00215.x>
- Allen, R. G., Pereira, L. S., Raes, D., & Smith, M. (1998). *Crop evapotranspiration-guidelines for computing crop water requirements-FAO irrigation and drainage paper 56*. FAO Rome.
- Boyd, M. J., Bufill, M. C., & Knee, R. M. (1993). Pervious and impervious runoff in urban catchments. *Hydrological Sciences Journal*, 38(6), 463–478. <https://doi.org/10.1080/0262669309492699>
- Chen, H., Huang, J. J., Liang, H., Wang, W. M., Li, H., Wei, Y. Z., Jiang, A. Z., & Zhang, P. W. (2023). Can evaporation from urban impervious surfaces be ignored? *Journal of Hydrology*, 616, 128582. <https://doi.org/10.1016/j.jhydrol.2022.128582>
- Chen, Y., Lei, T. J., Xia, J. Z., Tu, Y., Wang, Y. D., & Wang, Z. L. (2022). Application of a multiple model integration framework for mapping evapotranspiration with high spatial-temporal resolution in the Haihe River basin China. *Ecological Indicators*, 145, 109661. <https://doi.org/10.1016/j.ecolind.2022.109661>
- Cheng, Y. Y., & Byun, D. W. (2008). Application of high resolution land use and land cover data for atmospheric modeling in the Houston-Galveston metropolitan area, part I: Meteorological simulation results. *Atmospheric Environment*, 42(33), 7795–7811. <https://doi.org/10.1016/j.atmosenv.2008.04.055>
- Cleugh, H. A., Bui, E. N., Mitchell, V. G., Xu, J., Grimmond, C. S. B., & Simon, D. A. P. (2005). *Evapotranspiration in urban water balance models: A methodological framework* (pp. 2012–2018). International Congress on Modelling and Simulation (MODSIM05).
- Dams, J., Dujardin, J., Reggers, R., Bashir, I., Canters, F., & Batelaan, O. (2013). Mapping impervious surface change from remote sensing for hydrological modeling. *Journal of Hydrology*, 485, 84–95. <https://doi.org/10.1016/j.jhydrol.2012.09.045>
- Grimmond, C. S. B., & Oke, T. R. (1991). An evapotranspiration-interception model for urban areas. *Water Resources Research*, 27(7), 1739–1755. <https://doi.org/10.1029/91WR00557>
- Guo, Y., & Shen, Y. J. (2015). Quantifying water and energy budgets and the impacts of climatic and human factors in the Haihe River Basin, China: 1. Model and validation. *Journal of Hydrology*, 528, 206–216. <https://doi.org/10.1016/j.jhydrol.2015.06.039>
- Huang, H. B., Chen, P. M., Xu, X. Q., Liu, C. X., Wang, J., Liu, C., Clinton, N., & Gong, P. (2022). Estimating building height in China from ALOS AW3D30. *ISPRS Journal of Photogrammetry and Remote Sensing*, 185, 146–157. <https://doi.org/10.1016/j.isprsjprs.2022.01.022>
- Järvi, L., Grimmond, C. S. B., & Christen, A. (2011). The surface urban energy and water balance scheme (SUEWS): Evaluation in Los Angeles and Vancouver. *Journal of Hydrology*, 411(3–4), 219–237. <https://doi.org/10.1016/j.jhydrol.2011.10.001>
- Kokkonen, T. V., Grimmond, C. S. B., Christen, A., Oke, T. R., & Jarvi, L. (2018). Changes to the water balance over a century of Urban development in two neighborhoods: Vancouver, Canada. *Water Resources Research*, 54(9), 6625–6642. <https://doi.org/10.1029/2017WR022445>
- Kuang, W. H., Liu, J. Y., Zhang, Z. X., Lu, D. S., & Xiang, B. (2013). Spatio-temporal dynamics of impervious surface areas across China during the early 21st century. *Chinese Science Bulletin*, 58(14), 1691–1701. <https://doi.org/10.1007/s11434-012-5568-2>
- Li, M. M., Koks, E., Taubenböck, H., & van Vliet, J. (2020). Continental-scale mapping and analysis of 3D building structure. *Remote Sensing of Environment*, 245, 111859. <https://doi.org/10.1016/j.rse.2020.111859>
- Li, X., Koh, T., Panda, J., & Norford, L. K. (2016). Impact of urbanization patterns on the local climate of a tropical city, Singapore: An ensemble study. *Journal of Geophysical Research: Atmospheres*, 121(9), 4386–4403. <https://doi.org/10.1002/2015JD024452>
- Liu, X., Li, X. X., Harshan, S., Roth, M., & Velasco, E. (2017). Evaluation of an urban canopy model in a tropical city: The role of tree evapotranspiration. *Environmental Research Letters*, 12(9), 094008. <https://doi.org/10.1088/1748-9326/aa7ee7>
- Mahat, V., Tarboton, D. G., & Molotch, N. P. (2013). Testing above- and below-canopy representations of turbulent fluxes in an energy balance snowmelt model. *Water Resources Research*, 49, 1107–1122. <https://doi.org/10.1002/wrcr.20073>
- Mansell, M. R. F., & Rollet, F. (2009). The effect of surface texture on evaporation, infiltration and storage properties of paved surfaces. *Water Science & Technology*, 60(1), 71–76. <https://doi.org/10.2166/wst.2009.323>
- Masson, V. (2000). A physically-based scheme for the urban energy budget in atmospheric models. *Boundary-Layer Meteorology*, 94(3), 357–397. <https://doi.org/10.1023/A:1002463829265>
- Meili, N., Manoli, G., Burlando, P., Bou-Zeid, E., & Fatichi, S. (2020). An urban ecohydrological model to quantify the effect of vegetation on urban climate and hydrology (UT&C v1.0). *Geoscientific Model Development*, 13(1), 335–362. <https://doi.org/10.5194/gmd-13-335-2020>
- Minnig, M., Moeck, C., Radny, D., & Schirmer, M. (2018). Impact of urbanization on groundwater recharge rates in Dübendorf, Switzerland. *Journal of Hydrology*, 563, 1135–1146. <https://doi.org/10.1016/j.jhydrol.2017.09.058>
- Montzka, C., Canty, M., Kunkel, R., Menz, G., Vereecken, H., & Wendland, F. (2008). Modelling the water balance of a mesoscale catchment basin using remotely sensed land cover data. *Journal of Hydrology*, 353(3–4), 322–334. <https://doi.org/10.1016/j.jhydrol.2008.02.018>
- Moravej, M., Renouf, M. A., Lam, K. L., Kenway, S. J., & Urich, C. (2020). Site-scale Urban water mass balance assessment (SUWMB) to quantify water performance of urban design-technology-environment configurations. *Water Research*, 188, 116477. <https://doi.org/10.1016/j.watres.2020.116477>
- Mushimiyima, C., Liu, L. L., Yang, Y. H., Li, H. L., Wang, L. N., Sheng, Z. P., & Itangishaka, A. C. (2023). Drivers of evapotranspiration increase in the Baiyangdian catchment. *Chinese Journal of Eco-Agriculture*, 31(4), 598–607. <https://doi.org/10.12357/cjea.20220121>

- Oke, T. R. (1976). The distinction between canopy and boundary-layer urban heat islands. *Atmosphere*, 14(4), 268–277. <https://doi.org/10.1080/00046973.1976.9648422>
- Omidvar, H., Song, J., Yang, J., Arwatz, G., Wang, Z. H., Hultmark, M., Hultmark, M., Kaloush, K., & Bou-Zeid, E. (2018). Rapid modification of urban land surface temperature during rainfall. *Water Resources Research*, 54, 4245–4264. <https://doi.org/10.1029/2017WR022241>
- Ramamurthy, P., & Bou-Zeid, E. (2014). Contribution of impervious surfaces to urban evaporation. *Water Resources Research*, 50(4), 2889–2902. <https://doi.org/10.1002/2013WR013909>
- Sarkar, A., & De Ridder, K. (2011). The urban heat Island intensity of Paris: A case study based on a simple urban surface parametrization. *Boundary-Layer Meteorology*, 138(3), 511–520. <https://doi.org/10.1007/s10546-010-9568-y>
- Shao, R., Wang, Y., Shao, W., & Ni, G. H. (2022). Assessing the synergistic modulation of evapotranspiration by global impervious surface and vegetation changes. *Agricultural and Forest Meteorology*, 327, 109194. <https://doi.org/10.1016/j.agrformet.2022.109194>
- Silvennoinen, S., Taka, M., Yli-Pelkonen, V., Koivusalo, H., Ollikainen, M., & Setala, H. (2017). Monetary value of urban green space as an ecosystem service provider: A case study of urban runoff management in Finland. *Ecosystem Services*, 28, 17–27. <https://doi.org/10.1016/j.ecoser.2017.09.013>
- Strohbach, M. W., Doring, A. O., Mock, M., Sedrez, M., Mumm, O., Schneider, A. K., Webers, S., & Schroder, B. (2019). The “hidden urbanization”: Trends of impervious surface in low-density housing developments and resulting impacts on the water balance. *Frontiers in Environmental Science*, 7, 29. <https://doi.org/10.3389/fenvs.2019.00029>
- Sunde, M. G., He, H. S., Hubbart, J. A., & Urban, M. A. (2018). An integrated modeling approach for estimating hydrologic responses to future urbanization and climate changes in a mixed-use midwestern watershed. *Journal of Environmental Management*, 220, 149–162. <https://doi.org/10.1016/j.jenvman.2018.05.025>
- Wagner, P. D., Bhallamudi, S. M., Narasimhan, B., Kantakumar, L. N., Sudheer, K. P., Kumar, S., Schneider, K., & Fiener, P. (2016). Dynamic integration of land use changes in a hydrologic assessment of a rapidly developing Indian catchment. *Science of the Total Environment*, 539, 153–164. <https://doi.org/10.1016/j.scitotenv.2015.08.148>
- Wang, H. N., Lv, X. Z., & Zhang, M. Y. (2021). Sensitivity and attribution analysis based on the Budyko hypothesis for streamflow change in the Baiyangdian catchment, China. *Ecological Indicators*, 121, 107221. <https://doi.org/10.1016/j.ecolind.2020.107221>
- Wang, K. Y., Onodera, S., Saito, M., & Shimizu, Y. (2021). Long-term variations in water balance by increase in percent imperviousness of Urban regions. *Journal of Hydrology*, 602, 126767. <https://doi.org/10.1016/j.jhydrol.2021.126767>
- Wang, Z. H., Bou-Zeid, E., Au, S. K., & Smith, J. A. (2011). Analyzing the sensitivity of WRF's single-layer urban canopy model to parameter uncertainty using advanced Monte Carlo simulation. *Journal of Applied Meteorology and Climatology*, 50(9), 1795–1814. <https://doi.org/10.1175/2011JAMC2685.1>
- Wegehenkel, M., Heinrich, U., Uhlemann, S., Dunger, V., & Matschullat, J. (2006). The impact of different spatial land cover data sets on the outputs of a hydrological model—a modelling exercise in the ucker catchment, north-east Germany. *Physics and Chemistry of the Earth*, 31(17), 1075–1088. <https://doi.org/10.1016/j.pce.2006.07.006>
- Wiegels, R., Chapa, F., & Hack, J. (2021). High resolution modeling of the impact of urbanization and green infrastructure on the water and energy balance. *Urban Climate*, 39, 100961. <https://doi.org/10.1016/j.ulclim.2021.100961>
- Willuweit, L., & O'Sullivan, J. J. (2013). A decision support tool for sustainable planning of urban water systems: Presenting the dynamic Urban water simulation model. *Water Research*, 47(20), 7206–7220. <https://doi.org/10.1016/j.watres.2013.09.060>
- Wouters, H., Demuzere, M., Ridder, K. D., & Lipzig, N. P. M. (2015). The impact of impervious water-storage parametrization on urban climate modelling. *Urban Climate*, 11, 24–50. <https://doi.org/10.1016/j.ulclim.2014.11.005>
- Wu, W. B. (2023a). CNBH-10 m: A first Chinese building height at 10 m resolution [computer software]. Zenodo. <https://doi.org/10.5281/zenodo.7923866>
- Wu, W. B. (2023b). CNBH-10 m: A first Chinese building height at 10 m resolution [Data set]. Remote Sensing of Environment (Updated in April 2023, 291, 113578). Zenodo. <https://doi.org/10.5281/zenodo.7923866>
- Wu, W. B., Ma, J., Banzhaf, E., Meadows, M. E., Yu, Z. W., Guo, F. X., Sengupta, D., Cai, X. X., & Zhao, B. (2023). A first Chinese building height estimate at 10 m resolution (CNBH-10 m) using multi-source earth observations and machine learning. *Remote Sensing of Environment*, 291, 113578. <https://doi.org/10.1016/j.rse.2023.113578>
- Yang, J., & Huang, X. (2022). The 30 m annual land cover datasets and its dynamics in China from 1990 to 2021. *Earth System Science Data*, 13(1), 3907–3925. <https://doi.org/10.5281/zenodo.5816591>
- Yang, W., & Yang, Z. F. (2014). Analyzing hydrological regime variability and optimizing environmental flow allocation to lake ecosystems in a sustainable water management framework: Model development and a case study for China's Baiyangdian watershed. *Journal of Hydrologic Engineering*, 19(5), 993–1005. [https://doi.org/10.1061/\(ASCE\)HE.1943-5584.0000874](https://doi.org/10.1061/(ASCE)HE.1943-5584.0000874)
- Zhang, Y., Xia, J., Yu, J., Randall, M., Zhang, Y. C., Pan, X. Y., Zhao, T. T. G., Zhai, X. Y., & Shao, Q. X. (2018). Simulation and assessment of urbanization impacts on runoff metrics: Insights from landuse changes. *Journal of Hydrology*, 560, 247–258. <https://doi.org/10.1016/j.jhydrol.2018.03.031>
- Zhou, F., Xu, Y., Chen, Y., Xu, C. Y., Gao, Y. Q., & Du, J. K. (2013). Hydrological response to urbanization at different spatio-temporal scales simulated by coupling of CLUE-S and the SWAT model in the Yangtze River Delta region. *Journal of Hydrology*, 485, 113–125. <https://doi.org/10.1016/j.jhydrol.2012.12.040>
- Zhou, J. J., Liu, J. H., Chu, Q., Wang, H., Shao, W. W., Luo, Z. R., & Zhang, Y. X. (2021). Mechanisms and empirical modeling of evaporation from hardened surfaces in urban areas. *International Journal of Environmental Research and Public Health*, 18(4), 1790. <https://doi.org/10.3390/ijerph18041790>
- Zhou, J. J., Liu, J. H., Yan, D. Y., Wang, H., Wang, Z. J., Shao, W. W., & Luan, Y. (2019). Dissipation of water in urban area, mechanism and modelling with the consideration of anthropogenic impacts: A case study in Xiamen. *Journal of Hydrology*, 570, 356–365. <https://doi.org/10.1016/j.jhydrol.2018.12.054>
- Zipper, S. C., Schatz, J., Kucharik, C. J., & Loheide, S. P. (2017). Urban heat Island-induced increases in evapotranspirative demand. *Geophysical Research Letters*, 44(2), 873–881. <https://doi.org/10.1002/2016GL072190>

## SUPPORTING INFORMATION

Additional supporting information can be found online in the Supporting Information section at the end of this article.

**How to cite this article:** Liu, X., Mo, X., Liu, S., & Hu, S. (2024). Spatiotemporal distribution and influencing factors of impervious surface evaporation in the Baiyangdian catchment from 1980 to 2020. *Hydrological Processes*, 38(1), e15059. <https://doi.org/10.1002/hyp.15059>